# ASCAT IB: A radar-based vegetation optical depth retrieved from the ASCAT scatterometer satellite

Xiangzhuo Liu, Jean-Pierre Wigneron, Lei Fan, Frédéric Frappart, Philippe Ciais, Nicolas Baghdadi, Mehrez Zribi, Thomas Jagdhuber, Xiaojun Li, Mengjia Wang, et al.

# ASCAT IB: A radar-based vegetation optical depth retrieved from the ASCAT scatterometer satellite

Xiangzhuo Liu[a], Jean-Pierre Wigneron[a,*], Lei Fan[b], Frédéric Frappart[a,c], Philippe Ciais[d], Nicolas Baghdadi[e], Mehrez Zribi[f], Thomas Jagdhuber[g,h], Xiaojun Li[a], Mengjia Wang[i,a], Xiaojing Bai[j], Christophe Moisy[a]

a INRAE, UMR1391 ISPA, Université de Bordeaux, F-33140, Villenave d'Ornon, France

b Chongqing Jinfo Mountain Karst Ecosystem National Observation and Research Station, School of Geographical Sciences, Southwest University, Chongqing 400715, China

c Laboratoire d'Etudes en Géophysique et Océanographie Spatiales (LEGOS), 31400, Toulouse, France

d Laboratoire des Sciences du Climat et de l'Environnement, CEA/CNRS/UVSQ/Université Paris Saclay, Gif-sur-Yvette, France;

e IRSTEA, TETIS, Université of Montpellier, 500 rue François Breton, CEDEX 5, 34093 Montpellier, France

f CESBIO, Université de Toulouse, CNRS/UPS/IRD/CNES, 18 av. Edouard Belin, bpi 2801, CEDEX 9, 31401 Toulouse, France

g German Aerospace Center, DLR Microwaves and Radar Institute, P.O. BOX 1116, 82234 Wessling, Germany

h University of Augsburg, Institute of Geography, 86159 Augsburg, Germany.

i State Key Laboratory of Remote Sensing Science, Faculty of Geographical Science, Beijing Normal University, Beijing 100875, China

j School of Hydrology and Water Resources, Nanjing University of Information Science & Technology, Nanjing 210044, China

*Corresponding Author: J.-P. Wigneron (jean-pierre.wigneron@inrae.fr)

## Abstract:

Vegetation optical depth (VOD), as a microwave-based vegetation index for vegetation water and biomass content, is increasingly used to study the impact of global climate and environmental changes on vegetation. Currently, VOD is mainly retrieved from passive microwave data and few studies focused on VOD retrievals from active microwave data. The Advanced SCATterometer (ASCAT) provides long-term C-band backscatter data at Vertical-Vertical (VV) polarization. In this study, a new ASCAT INRAE Bordeaux (IB) VOD (hereafter, IB VOD), was developed based on the Water Cloud Model (WCM) coupled with the Ulaby linear model for soil backscattering. The main features of IB VOD are that (i) the ERA5-Land soil moisture (SM) dataset was used as an auxiliary SM dataset in the retrievals, (ii) pixel-based soil model parameters were mapped using Random Forest (RF), and (iii) the vegetation model parameter was calibrated for each day. The IB VOD product was retrieved over Africa during 2015-2019, and its performances were evaluated in space and time by comparing with aboveground biomass (AGB), lidar tree height (TH), normalized difference vegetation index (NDVI), enhanced vegetation index (EVI) and leaf area index (LAI). Results were inter-compared with three other VOD products at the same frequency. In terms of spatial correlation with AGB (R = 0.92) and TH (R = 0.89), IB VOD outperforms the other VOD products, suggesting IB VOD has a strong ability to capture spatial patterns of AGB and TH. By

comparing all VOD products against NDVI, EVI and LAI, we found that the highest temporal correlation with NDVI (EVI, LAI) was obtained with IB VOD over 29.94 % (36.65 %, 30.19 %) of the study region. Considering all three vegetations indices, highest temporal correlation values with IB VOD could be particularly noted for deciduous broadleaf forests, woody savannas and savannas.

**Keywords: VOD, ASCAT, active microwave, Africa, biomass, tree height, NDVI, EVI, LAI**

# 1. Introduction:

Vegetation optical depth (VOD), a measure of extinction effects of the microwave (passive or active) radiations by the vegetation canopy, is related to the vegetation water content (VWC) (Wigneron et al., 2017). VOD has been used in many applications in the fields of global climate and environmental changes. For example, several studies have investigated carbon dynamics in the pantropics (Brandt et al., 2018; Fan et al., 2019; Qin et al., 2021; Wigneron et al., 2020) and at the global scale (Liu et al., 2015; Liu et al., 2013), vegetation phenology (Jones et al., 2011), the global isohydricity variations and drought detection (Konings and Gentine, 2017; Rao et al., 2019), and burned area trends and fire risks (Fan et al., 2018; Forkel et al., 2019). VOD has also been used to estimate the gross primary production (GPP) (Teubner et al. 2018), the crop yields (Chaparro et al., 2018; Patton and Hornbuckle, 2013) and asymmetry patterns in inter-annual productivity (Al-Yaari et al., 2020).

Several VOD datasets used in the above-mentioned studies are mainly derived from passive microwave sensors operating at different frequencies (Frappart et al., 2020). Those datasets

include the high-frequencies (C-/X-/Ku- band) VOD (Du et al., 2017; Karthikeyan et al., 2019, 2020; Owe et al., 2008) from AMSR-E (the Advanced Microwave Scanning Radiometer, July 2002-2008) (Koike et al., 2004) and its successor, AMSR2 (the Advanced Microwave Scanning Radiometer 2, 2012-present) (Imaoka et al., 2012) and the low frequency VOD at L-band (L-VOD) (Feldman et al., 2018; Fernandez-Moran et al., 2017; Konings et al., 2016; Wigneron et al., 2017, 2021) from the Soil Moisture and Ocean Salinity (SMOS) (Kerr et al., 2010) and Soil Moisture Active Passive (SMAP) (Entekhabi et al., 2010) satellites. In addition, a long-term VOD product merging the different high frequency datasets was also released (Liu et al., 2011; Moesinger et al., 2020). Although different passive VOD products have been widely used in different applications, they still have some deficiencies. For instance, the time period of each product is rather short in terms of years (the longest acquisition period of the different sensors is ~ 11 years for SMOS), and the spatial resolution of the VOD data is coarse (~25 km). Moreover, the data quality from passive sensors (especially at low frequency (L-band)) are more likely to be affected by radio frequency interference (RFI) (Li et al., 2021).

Active microwave data can provide long-term records (Advanced SCATterometer (ASCAT) provided data from 2007 with a spatial resolution of 25-50 km) and high spatial resolution data (~10 m for Sentinel-1 from 2014) with less RFI influence than for passive microwave sensors, resulting in high quality products. Active microwave sensors can also observe different information from the vegetation and soil compared with passive sensors (Dente et al. 2014; Li et al. 2017; Teubner et al. 2018). In previous studies, the active backscatter observations have been mainly utilized in the retrievals of ocean winds (Hersbach et al., 2007; Stoffelen and Anderson, 1997) and soil moisture (SM) (Bai et al., 2017; Konings et al., 2017; Wagner et al., 1999b) but very few studies focus on VOD retrievals. To our knowledge, there are only preliminary results obtained from Sentinel-1 in southern France (El Hajj et al., 2019) and one global active VOD dataset (hereafter, ASCAT V16 VOD) developed by Vreugdenhil et al.

(2016) from ASCAT observations. Two parameters were used in the retrieval of ASCAT V16 VOD. The first one is the maximum range of the backscatter values over bare soils that are related to SM changes. The setting of this parameter was based on the Koppen-Geiger climate classification map (Kottek et al., 2006) and the parameter was set to a constant value over most regions except for the desert climate zone. The second parameter is the difference between the wet and dry references that are obtained from the historically wettest and driest backscatter measurements. This product is not yet public, and it has not been evaluated in detail in the literature (Vreugdenhil et al., 2017, 2020).

To retrieve VOD from the ASCAT observations, two challenges need to be solved: (1) selecting suitable models which account for the vegetation (mainly through the VOD parameter) and bare soil (mainly through SM and roughness) effects in the simulation of the ASCAT C-band backscatter. Several bare soil and vegetation backscatter models have been proposed in the literature. Most popular bare soil backscatter models include the Ulaby linear model (Ulaby et al., 1978), the Oh model (Oh et al., 1992), the Dubois model (Dubois et al., 1995), the integral equation model (IEM) (Fung et al., 1992) and the advanced IEM (AIEM) (Chen et al., 2003). Concerning the vegetation backscatter models, the most widely used models are the water cloud model (WCM) (Attema and Ulaby, 1978), the Michigan microwave canopy scattering (MIMICS) model (Ulaby et al., 2007) and the Tor Vergata model (Bracaglia et al., 1995). (2) The second issue is to deal with the ill-posed problem in retrieving both VOD and SM (Wigneron et al., 2000). ASCAT allows multi-angular observations, but the use of this information requires careful implementation (Pfeil et al., 2020). To integrate multi-angular information, ASCAT backscatter measurements (VV polarization) are normalized to the incidence angle ($\theta$) of 40 degrees (Hahn et al., 2017; Naeimi et al., 2009). Therefore, retrieving simultaneously SM and VOD using mono-angle and mono-polarization observations may be difficult.

Here we aim at retrieving VOD (0.25 degree x 0.25 degree) from ASCAT backscatter data (hereafter, INRAE Bordeaux (IB) VOD) over Africa from 2015 to 2019. The WCM (for vegetation scattering components) and the Ulaby linear model (for soil scattering) were chosen to simulate ASCAT backscatter as they have good computational efficiency due to analytical solutions and performant simulation accuracy at large scales (Lievens et al., 2017; Shamambo et al., 2019). To overcome the ill-posed problem of retrieving both VOD and SM from mono-angular ASCAT observations, we focused on retrieving only the VOD parameter and we used an existing SM product as input parameter (Baur et al., 2019; Lievens et al., 2017; Shamambo et al., 2019). The observation time of the SM data derived from other EO sensors (such as SMOS, SMAP or AMSR2 SM) is different from that of ASCAT and the time period of those products is too short (for instance, SMOS was launched end of 2009). Therefore, our retrieval algorithm used model-based SM data from the ERA5-Land product as a known SM input of the retrieval algorithm. For a first evaluation analysis, this study is conducted over Africa as this continent has a large variety of vegetation and climate conditions. Following Li et al. (2021), several vegetation parameters and indices (Aboveground Biomass (AGB), Lidar tree height (TH), the Moderate Resolution Imaging Spectroradiometer (MODIS) normalized difference vegetation index (NDVI) and Enhanced Vegetation Index (EVI) and leaf area index (LAI)) were used to evaluate the performance of IB VOD in space and time. In addition, to understand the performance of IB VOD, we made a comparison between IB VOD and three other VOD products at C-band.

This study is organized as follows: Section 2 introduces the datasets. Section 3 presents the models including WCM, Ulaby linear model and the method used for model calibration. In Section 4, we present the results of the calibrated model and the evaluation of IB VOD. Discussion and conclusion are provided in Section 5 and 6.

# 2. Data

Several datasets were used in this study. The main features and purpose of each dataset are shown in Table 1. More details are given as follows.

## 2.1 ASCAT backscatter data

The Advanced SCATterometer (ASCAT) (Figa-Saldaña et al., 2014) is an active microwave sensor that measures VV backscatter with incidence angles from 25 to 65 degrees at C-band (5.255 GHz) (Wagner et al., 2013). ASCAT is carried by the Meteorological Operational Satellite Program of Europe (Metop) series of satellites. This series includes three satellites which were launched on 19 October 2006 (MetOp-A), 17 September 2012 (MetOp-B) and 7 November 2018 (MetOp-C), respectively. Each satellite flew in a sun-synchronous orbit and overpassed the surface twice a day near the Local Sidereal Time (LST) 09:30 (descending) and 21:30 (ascending).

The European Organization for the Exploitation of Meteorological Satellites (EUMETSAT) provides users with two kinds of backscatter data at a spatial resolution of 25 km or 50 km: level one (L1) original data and level two (L2) processed data. The L2 data are normalized by using a second-order polynomial function describing the relationship between incidence angle and backscatter (Wagner et al., 1999a), and are included in the soil moisture datasets. The data are stored in a discrete global grid (Swath Grid format); the grid spacing of the 50 km data is 25 km, and 12.5 km for the 25 km data.

Five years (2015-2019) L2 MetOp-A backscatter (25 km x 25 km) data normalized at an incidence of 40 degrees were used in the present study. As there is usually a lower vegetation water stress in the morning making descending VOD data more suitable to monitor biomass (Frappart et al., 2020), only observations from the descending orbits were used. 'Low quality' data were masked through the quality flags (snow cover, frozen soil, topography and wetland

probability) (Lievens et al., 2017), and then we used the inverse distance weighting algorithm to average the backscatter data to the WGS 84 latitude/longitude format with a spatial resolution of 0.25 degree (Lievens et al., 2017).

## 2.2 ERA5-Land Soil Moisture data

The ERA5-Land Soil Moisture (SM) dataset from the topsoil layer (layer 1, 0-7 cm) was used in this study. ERA5-Land SM is a reanalysis dataset modelled by the European Centre for Medium-Range Weather Forecasts (ECMWF) surface model (Berrisford et al., 2011) with an enhanced resolution compared to ERA5 SM. The data are hourly and have a spatial resolution of 0.1 degree x 0.1 degree (around 10 km x 10 km). An evaluation of ERA5-Land SM by using the International Soil Moisture Network (ISMN, Dorigo et al., 2021) in situ measurements at the global scale suggested that it has an overall good performance (R = 0.72~0.76, ubRMSE = 0.05 $m^3/m^3$) (Beck et al., 2020; Chen et al., 2021). ERA5-Land SM modelled at the local time of 09:00 am, which is close to the time of the ASCAT observation, were inputs to the water cloud model (WCM) used to retrieve IB VOD. The data were resampled to the 0.25 degree resolution by area-weighted averaging.

## 2.3 Soil and terrain data

The soil and terrain data have an important impact on the soil moisture and the signal acquired from the microwave observations (Guio Blanco et al., 2018; Ma et al., 2015). Therefore, we considered using those two kinds of data in the calibration of the soil model parameters.

The soil data include the soil property and the soil temperature (ST) data. The applied soil property data were obtained from the SoilGrid250m dataset (Hengl et al., 2017). This dataset was generated by the machine learning method at 250 m spatial resolution and seven standard depths. In this study, we used the average value of the first (0 cm, corresponding to the surface) and second depth (5 cm) of each soil property. More details about the dataset and the method

used to compute average data from different depths were described in Hengl et al. (2017). Fifteen SoilGird250m parameters were used in the present study and are described in Appendix Table 1. The ST data were obtained from ERA5-Land, for the same soil layer and at the same time as ERA5-Land SM.

The terrain parameters were obtained from a digital elevation model (DEM). The DEM data used here is the Global Multi-resolution Terrain Elevation Data (GMTED) 2010 at a spatial resolution of 1 km (Danielson and Gesch, 2011). The SAGA (System for Automated Geoscientific Analyses) GIS software (Conrad et al., 2015) was used to calculate six terrain parameters: Slope, Terrain Surface Convexity (TSC), Terrain Surface Texture (TST), Terrain Ruggedness Index (TRI), Plan Curvature (PlanCur) and Profile Curvature (ProfCur). All terrain parameters used in this study are given in Appendix Table 2.

## 2.4 Vegetation variables used for validation

As there is no large-scale in situ dataset that can be used for the validation of VOD (Li et al. 2020, 2021), AGB (Saatchi and CCI AGB), Lidar tree height (TH) (Simard and Potapov tree height) and vegetation indices (MODIS NDVI, EVI and LAI) were used as the benchmark to assess the performance of IB VOD (Fernandez-Moran et al., 2017; Li et al., 2021). The rationale for using these different vegetation parameters is given in the following. VOD is related to the vegetation water content which is determined by the quantity of vegetation (parameterized by biomass) and the vegetation water status (parameterized by the vegetation moisture content). VOD can thus provide information on AGB and on the vegetation water status and stress of the vegetation canopy (Frappart et al., 2020; Togliatti et al., 2019). As presented above, VOD is directly related to AGB and many studies have shown that the yearly average of C-band VOD can be used to estimate AGB (Chaparro et al., 2019; Liu et al., 2015; Tian et al., 2016). Therefore, spatial correlation between the yearly average of IB VOD and AGB was computed to assess the performance of VOD. Similarly, the total amount of vegetation matter (AGB) is

dependent on the vegetation height (Asner et al., 2012). For instance, one of the key objectives of the recent Global Ecosystem Dynamics Investigation (GEDI) lidar instrument is to monitor the aboveground carbon balance from accurate estimates of the vegetation height (Duncanson et al., 2020). Thus, the comparison of VOD with tree height data was also conducted to verify the expected dependence of VOD on AGB. Several studies have also shown that the temporal dynamics of VOD is a good indicator of the vegetation phenology (Lawrence et al., 2014, Jones et al., 2011, 2014) as monitored from optical vegetation indices (NDVI, EVI and LAI). Therefore, these different vegetation indices (VIs) were also used in this study to assess the performance of VOD in temporal terms. More generally, note that similarly to what is done here, many studies evaluating the VOD products have been based on AGB, TH, NDVI, EVI and LAI (Grant et al., 2016; Li et al., 2020, 2021; Rodríguez-Fernández et al., 2018; Tian et al., 2016, 2018). More details about these data sets are presented in Appendix A. All those data sets were resampled to the spatial resolution of the ASCAT product (0.25 degree) by arithmetic average.

## 2.5 C-band VOD products used for inter-comparison

To evaluate the quality of the IB VOD product, we compared it with other VOD products retrieved at the same frequency (C-band). In this comparison, we used three datasets: two public passive VOD datasets and one active VOD dataset (Frappart et al., 2020). The two passive VOD datasets are AMSR2 VOD (Owe et al., 2008) and Vegetation Optical Depth Climate Archive (VODCA) VOD (Moesinger et al., 2020). The retrieval algorithm of the two products is the Land Parameter Retrieval Model (LPRM) but a different version (version 5 (V5)) was used for AMSR2, while Version 6 (V6) was used for VODCA (Li et al., 2020). VODCA LPRM V6 VOD was rescaled via cumulative distribution function matching using AMSR-E VOD as the reference. AMSR2 LPRM V5 VOD is available at the Goddard Earth Sciences Data and Information Services Center (GES DISC) website. VODCA LPRM V6 is available at

https://doi.org/10.5281/zenodo.2575599. The active VOD dataset is the ASCAT V16 VOD (Vreugdenhil et al., 2016). As there is no available website to download the dataset, the ASCAT V16 VOD dataset was produced by the authors of this study based on the published algorithm (Vreugdenhil et al., 2016).

## 2.6 Ancillary vegetation dataset

Two ancillary vegetation datasets were used in this study. The MODIS-based land cover map over Africa was used to assist in soil model parameter calibration and to interpret the VOD inter-comparison results as a function of land cover types. This land cover map is produced by combining the 500 m MCD12Q1 (Collection 6) over 2017 in the International Geosphere-Biosphere Programme (IGBP) scheme (Sulla-Menashe and Friedl, 2019). In addition, the tree cover percentage (TCP) data from MOD44B Vegetation Continuous Fields (VCF) product (DiMiceli et al., 2015) over 2017 were used to assist in calibrating the soil and vegetation model parameters.

The TCP data were re-scaled to the 0.25 degree grid by arithmetic averaging, and the land cover type with the maximum cover fraction in each 0.25 degree grid was considered as the land cover type of the pixel (Fernandez-Moran et al., 2017).

257 **Table 1.** Overview of all datasets used in this study

| Dara Name | Spatial sampling | Temporal period | Time period | Purpose | Reference |
|---|---|---|---|---|---|
| ASCAT backscatter data | 12.5km | Daily | 2015-2019 | model input and calibration | https://archive.eumetsat.int/ |
| ERA5-Land soil moisture data | 0.1° | Hourly | 2015-2019 | model input and calibration | https://cds.climate.copernicus.eu/ |
| ERA5-Land soil temperature data | 0.1° | Hourly | 2017 | model calibration | https://cds.climate.copernicus.eu/ |
| Soil property data | 250m | Yearly | / | model calibration | Hengl et al., 2017 |
| Terrain data | 1km | Yearly | / | model calibration | Danielson and Gesch, 2011 |
| MODIS land cover | 500m | Yearly | 2017 | model calibration | Sulla-Menashe and Friedl, 2019 |
| MODIS LAI | 500m | 8-day | 2015-2018 | model calibration and validation | Myneni et al., 2015 |
| MODIS VCF | 1km | Yearly | 2017 | model calibration | DiMiceli et al., 2015 |
| Saatchi AGB data | 1km | Yearly | 2015 | validation | Carreiras et al., 2017; Saatchi et al., 2011 |
| CCI AGB data | 100m | Yearly | 2017 | validation | Santoro and Cartus, 2019 |
| Simard tree height data | 1km | Yearly | 2005 | validation | Simard et al., 2011 |
| Potapov tree height data | 30m | Yearly | 2019 | validation | Potapov et al., 2020 |
| MODIS NDVI and EVI | 1km | 16-day | 2015-2018 | validation | Didan, 2015 |
| AMSR2 LPRM V5 VOD | 0.25° | Daily | 2015-2019 | inter-comparison | https://disc.gsfc.nasa.gov/ |
| VODCA LPRM V6 VOD | 0.25° | Daily | 2015-2018 | inter-comparison | https://doi.org/10.5281/zenodo.2575599 |
| ASCAT V16 VOD | 0.25° | Daily | 2015-2019 | inter-comparison | Vreugdenhil et al., 2016 |

258

# 3. Methodology

## 3.1 Water cloud model

The water cloud model (WCM) developed by Attema and Ulaby (1978) is a semi-empirical model used to simulate the radar backscatter signal from vegetation and bare soil land surfaces. In WCM, the total backscatter reflected by the vegetated-soil surface ($\sigma^{\circ}_{obs}$, in linear units) is decomposed into three components: the direct backscatter of vegetation ($\sigma^{\circ}_{vege}$, in linear units), the double-bounce backscatter between the vegetation canopy and the bare soil surface ($\sigma^{\circ}_{vege+soil}$, in linear units) and the direct backscatter from the soil surface attenuated by the vegetation canopy ($\sigma^{\circ}_{soil}$, in linear units). The attenuation effects of vegetation are parameterized by the vegetation transmissivity ($\gamma^2$) which can be computed from the incidence angle (θ, 40 degrees in this study) and VOD as given below:

$$\sigma^{\circ}_{obs} = \sigma^{\circ}_{vege} + \gamma^2 \sigma^{\circ}_{soil} + \sigma^{\circ}_{vege+soil} \quad (1)$$

With

$$\sigma^{\circ}_{vege} = AV_1 cos\theta \left(1-\gamma^2\right) \quad (2)$$

$$\gamma^2 = exp\left(-2VOD / cos\theta\right) \quad (3)$$

Where A is the vegetation canopy backscattering at the full cover (Bindlish and Barros, 2001) (the $V_1$ index can generally be set to one (Attema and Ulaby, 1978)).

To model the backscatter of the soil surface ($\sigma^{\circ}_{soil}$), we used a linear relationship (Eq. (4)) relating the soil backscatter ($\sigma^{\circ}_{soil(dB)}$, in dB) to soil moisture (*SM*). This simple model was proposed by Ulaby et al. (1978) and has been used in many studies (Hosseini et al., 2015; Lievens et al., 2017; Quesney, 2000).

$$\sigma^{\circ}_{soil(dB)} = 10log_{10}\sigma^{\circ}_{soil} = C + D*SM \quad (4)$$

Where C is the radar backscatter in very dry conditions ($SM$ ~ 0 $m^3/m^3$), and D parameterizes the sensitivity of the radar data to soil moisture.

Following Baghdadi et al. (2017) and Zribi et al. (2019), we neglected the $\sigma^{\circ}_{vege+soil}$ term and VOD can be computed as:

$$VOD = -\frac{1}{2}cos\theta \ln\left(\frac{\sigma^{\circ}_{obs} - Acos\theta}{10^{0.1(C+D*SM)} - Acos\theta}\right) \quad (5)$$

In this study, our objective was to retrieve VOD from ASCAT over the whole African continent. Therefore, the parameters A, C and D have to be calibrated over each pixel of Africa. We performed first the calibration of the soil parameters (C and D) by selecting spatial/temporal conditions for which the vegetation effects could be neglected and then we calibrated the vegetation parameter (A).

Note that, when vegetation is very dense, the vegetation transmissivity can be assumed to be zero ( $\gamma^2 = 0$ ) and Eq. (2) can be simplified and written as:

$$\sigma^{\circ}_{obs} = 10^{\frac{\sigma^{\circ}_{obs(dB)}}{10}} = \sigma^{\circ}_{vege} = A * cos\theta \quad (6)$$

And the value of A for very dense vegetation (VDV) conditions (referred to as $A_0$ ) can be computed very simply as:

$$A_0 = \sigma^{\circ}_{obs} / cos\theta \quad (7)$$

## 3.2 Soil model parameters (C and D) calibration

To calibrate the soil parameters (C and D), we first computed the values of the C and D parameters from the "bare soil" pixels where these parameters could be directly calibrated, and then we used the random forest approach to calibrate C and D for the pixels where this direct

calibration could not be done. The soil calibration was performed in the year 2017. The different steps are summarized in Fig. 1.

### *3.2.1 Step 1: "bare soil" pixels selection*

The purpose of step 1 is to select "bare soil" pixels. Only two cases where the observed backscatter can be assumed to originate totally from the soil (Wigneron et al., 2002) are considered, namely, either bare land without any vegetation cover throughout the year (case 1), or land covered by a certain degree of sparse dynamic vegetation (case 2).

The case 1 was defined here by considering two conditions: there is no MODIS LAI observation (*i.e.* LAI = Nan) throughout the year and the IGBP land cover type is "bare soil". When the pixels correspond to case 2, it means there is a period during which the vegetation is relatively sparse (*e.g.* before the vegetation development or after senescence). Following Parrens et al. (2016), the condition of sparse vegetation was defined as LAI lower than 0.5 $m^2$ $m^{-2}$.

Then the "bare soil" pixels were divided into two categories: pixels where $\sigma^{\circ}_{obs(dB)}$ is sensitive to soil moisture (SM) (category 1) and pixels where $\sigma^{\circ}_{obs(dB)}$ is in very dry conditions all the time, so that $\sigma^{\circ}_{obs(dB)}$ ~ constant (category 2).

More specifically, to distinguish pixels/dates corresponding to categories 1 and 2 we used the following criteria:

First, we extracted the time series of $\sigma^{\circ}_{obs(dB)}$ and soil moisture (SM) from, respectively, the ASCAT and ERA5 Land SM datasets for pixels/dates corresponding to the case 1 and 2. For category 1, the standard deviation of $\sigma^{\circ}_{obs(dB)}$ and SM (corresponding to the dates where LAI < 0.5 $m^2$ $m^{-2}$ or LAI=Nan) should be larger than 0.5 dB and 0.04 $m^3/m^3$, respectively, and the number of the $\sigma^{\circ}_{obs(dB)}$ data corresponding to these two cases should be larger than 30% of the whole number of backscatter observations. For category 2, the standard deviation of $\sigma^{\circ}_{obs(dB)}$

and SM should be lower than 0.5 dB and 0.04 $m^3/m^3$, respectively, and the number of SM data lower than 0.05 $m^3/m^3$ should be larger than 95% of the total number of backscatter observations.

This filtering step was mainly done to:

-identify the areas (category 1) with clear temporal changes in both $\sigma^{\circ}_{obs(dB)}$ and SM, so that we could compute a linear relationship between $\sigma^{\circ}_{obs(dB)}$ and SM (Eq. (4)), and

-distinguish very dry areas (category 2), where SM is almost constant and over which the value of $\sigma^{\circ}_{obs(dB)}$ in very dry conditions could be obtained.

### *3.2.2 Step 2: soil parameters computation for "bare soil" pixels*

In step 2, over the pixels corresponding to category 1, the slope (D) and intercept (C) of Eq. (4) were retrieved. Over the pixels corresponding to category 2, we retrieved only the intercept (C). For pixels corresponding to category 1, a linear regression between the time series of $\sigma^{\circ}_{obs(dB)}$ and SM was established and we only retained the values of C and D when the following conditions, ensuring a robust and physically-based linear relationship, were met:

(i) the correlation value (R) of the linear relationship between time series of $\sigma^{\circ}_{obs(dB)}$ and SM is positive,

(ii) the relationship is significant (p-value < 0.01)

For pixels corresponding to category 2, the C parameter was simply computed as the average value of the backscatter time series.

### *3.2.3 Step 3: soil parameters calibration for all pixels*

Based on the results of step 2 (where we computed the values of the C and D parameters from the pixels where these parameters could be determined), we used the corresponding soil property data (Appendix Table 1) and terrain data (Appendix Table 2) as predictors to train two

random forest (RF) regression models for the C and D parameters, separately. RF regression is a machine learning method that has the advantage to be a nonlinear and nonparametric method, and the contribution of each predictor to the target that is computed by the RF model is very useful for tuning the model. We implemented the RF analysis using the python *sklearn* package (Pedregosa et al., 2011) for each soil model parameter. The *GridSearchCV* function was used to find the optimal setting of the two RF parameters (*n_estimators* and *max_features*). Besides, there are 27 predictors for each soil model parameter and collinearity exists among them. In order to achieve a good model performance with fewer predictors, the Recursive Feature Elimination (RFE) method (Guyon et al., 2002) was used to select the predictors. After this training step, the trained random forest models allowed us to compute a map of the soil model parameters (C and D) over the whole of Africa by inputting the soil property and terrain maps of Africa.

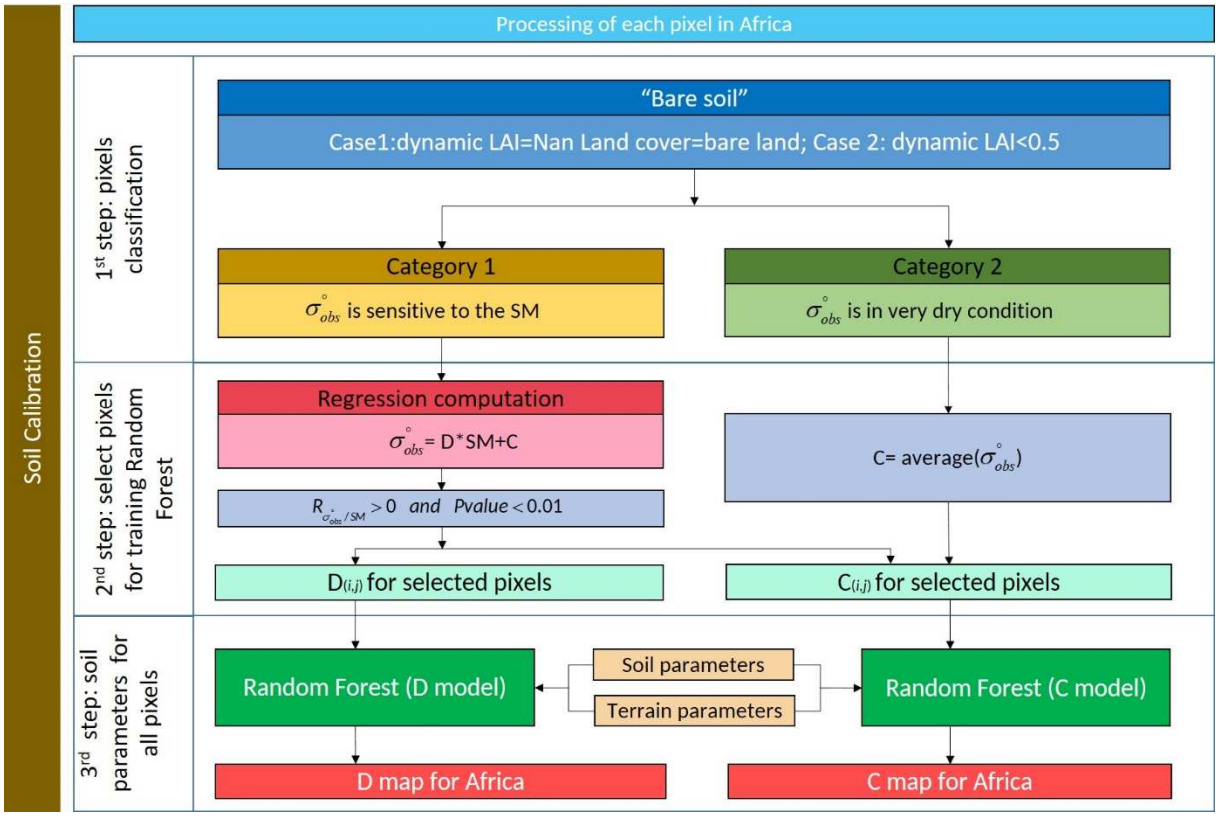


**Fig. 1.** Flowchart for computing the C and D map over Africa.

## 3.3 Vegetation model parameter (A) calibration

The dynamic vegetation parameter A of the WCM model was calibrated using the measured backscatter ($\sigma^{\circ}_{obs(dB)}$) over the very dense vegetated (VDV) region which was defined as the region where the percentage of tree cover in vegetation continuous fields (VCF) is larger than 75% (Santoro et al., 2015). Considering that the vegetation transmissivity is close to zero over VDV regions (Konings et al., 2017; Parrens et al., 2017), we assumed that the soil backscatter ($\sigma^{\circ}_{soil}$) is totally attenuated, meaning that the backscatter of vegetation ($\sigma^{\circ}_{vege}$) can be set equal to the measured backscatter ($\sigma^{\circ}_{obs}$, in linear units) as given in Eq. (6). Eq. (7), converted from Eq. (6), was used to compute $A_0(t)$ by spatial averaging all $A_0(i, j, t)$ values over all VDV pixels at *t* day.

In an initial step, we set $A(i, j, t)$ equal to $A_0(t)$ over all pixels (assuming all pixels have the same $A_0(t)$ value at date t). However, this assumption fails when $\sigma^{\circ}_{obs} > A_0(t)*cos\theta$, because in that case $10^{0.1(C+D*SM)} - Acos\theta$ is always negative and therefore VOD cannot be computed from Eq. (5). To overcome the issue, we divided the study area into two regions:

- Region 1 included all pixels where more than 50% of the $\sigma^{\circ}_{obs}$ data are lower than $A_0(t)*cos\theta$: it generally corresponds to pixels with sparse or low vegetation where relatively low $A(i, j, t)$ values were retrieved. In region 1, we set $A(i, j, t)$ equal to $A_0(t)$.
- Region 2 included all pixels where more than 50% of the $\sigma^{\circ}_{obs}$ data are higher or equal than $A_0(t)*cos\theta$: it generally corresponds to pixels with dense vegetation where high $A(i, j, t)$ values were retrieved. In region 2, we set $A(i, j, t)$ equal to $A_0^{95\%}(t)$ which is the 95th percentile of $A_0(i, j)$ over all VDV pixels at day *t*.

So, eventually, the value of $A(i, j)$ for each pixel on each day ($t$) in Africa was set simply as follows:

$$A(i,j,t) = \begin{cases} A_0(t), & region\ \ 1 \\ A_0^{95\%}(t), & region\ \ 2 \end{cases} \quad (8)$$

The flowchart for mapping the vegetation parameter is presented in Fig. 2.

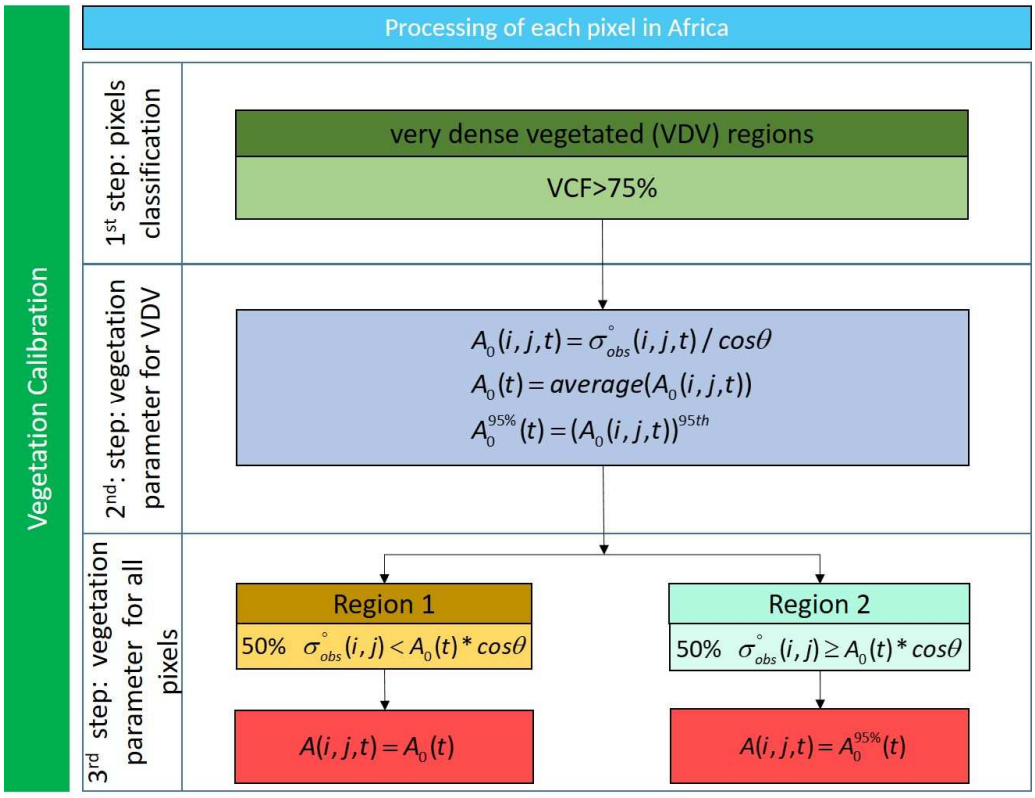


**Fig. 2.** Flowchart for computing the A map over Africa.

# 4. Result

This section is divided into two parts: the first concerns the results of the soil and vegetation parameters calibration, the second concerns the evaluation and inter-comparison of IB VOD with other products.

## 4.1 Calibration results of soil parameters

### *4.1.1 Computation results of C and D for "bare soil" pixels*

Based on the method defined in section 3.2.1, we extracted 1610 and 7524 pixels belonging, respectively, to category 1 ($\sigma^{\circ}_{obs(dB)}$ is sensitive to the soil moisture) and category 2 ($\sigma^{\circ}_{obs(dB)}$ is in very dry conditions all the time).

The computation of C and D was carried out for both categories 1 and 2. For the pixels belonging to category 1, the C and D values were derived based on Eq. (4). As $\sigma^{\circ}_{obs(dB)}$ increases with the increase in soil moisture, only the pixels that obtained a significant positive correlation (p-value<0.01) between $\sigma^{\circ}_{obs(dB)}$ and SM were kept. As a result, 78.39 % of the pixels (1262 pixels) were retained. For category 2, all pixels (7524 pixels) can be used to compute the C value. Together with the pixels retained for category 1 (1262 pixels), 8786 pixels were used to calibrate the C parameter.

The spatial distribution of the pixels used for the calibration of the C and D parameters is shown in Fig. 3 (a). We can see that the pixels used to calibrate the D value are located in the north, centre and south of Africa. Grassland, which represents 630 pixels (50.80 %), is the most common vegetation type among these pixels, then cropland with 302 pixels (23.93 %), followed by open shrubland with 298 pixels (23.61 %), and finally savanna, barren or sparsely vegetated, crop & natural vegetation mosaic with 26 pixels (2.06 %). Pixels in category 2 are mainly distributed in the Sahara Desert. The distribution of the retrieved C values can be well fitted with a Gaussian distribution, while that of the D values is better represented by a lognormal distribution (Fig. 3 (b, c)).

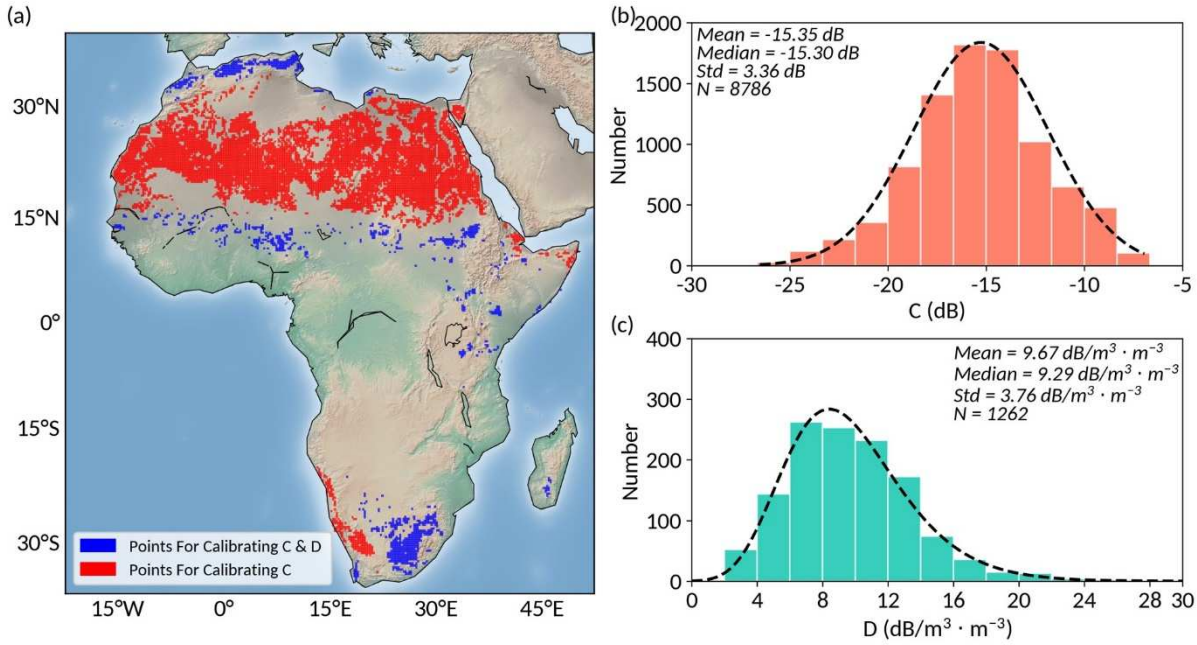


**Fig. 3.** (a) Spatial distribution of pixels used to calibrate the C (red and blue) and D (blue) soil parameters; and histograms of the retrieved (b) C and (c) D values.

### *4.1.2 Variable used for training the RF model*

In order to estimate the values of C and D over the whole of Africa, two random forest regression models were built. Based on the results of the *GridSearchCV*, we set the *n_estimators* equal to 1000 for the two RF models, and the value of the *max_features* equal to the number of the variables. The RFE algorithm was applied to the predictors of the selection experiments for each model. The selected predictors and their importance are shown in Fig. 4. The predictors that have higher importance mean that they can explain better the target (e.g. the retrieved C and D values).

Based on the RFE algorithm, 16 out of the 27 variables were selected to train the model used to map the C value, including 4 terrain parameters (importance weight of 30.42 %) and 12 soil property parameters (importance weight of 69.58 %). The top five variables by importance were the soil organic carbon density (Ocdens) (25.50 %), the standard deviation of elevation (dem_std) (12.63 %), the terrain ruggedness index (TRI) (7.05 %), the pH index measured in

water solution (Phihox) (6.25 %) and the terrain surface texture (TST) (6.21 %). Those five variables can explain around 58 % of the target. Similarly, to map the D value, we selected 16 variables consisting of 3 terrain parameters (importance weight of 16.46 %) and 13 soil property parameters (importance weight of 83.54 %). The top five variables by importance were the pH index measured in KCl solution (Phikcl) (17.83 %), the mean value of soil temperature (mean_ST) (7.84 %), the soil organic carbon stock (Ocstha) (6.62 %), the coefficient of variations of the soil temperature (cv_ST) (6.53 %) and the weight percentage of the sand particles (Sndppt) (6.19 %).

As presented in section 3.1, the C value corresponds to the radar backscatter in very dry conditions, and D represents the sensitivity of the radar data to soil moisture. Therefore, the C value is more related to terrain roughness and the D value is more related to the soil properties. The two RF models for the C and D values have different features. For instance, the contribution of the terrain parameters (related to topography) in the C value model is, as expected, larger than that in the D value model. Conversely, similar aspects were found between the two RF models. For instance, the predictor related to the soil organic carbon is in the top five predictors for the two models: Ocdens is the most important variable in the C value model, while Ocstha ranks in the third place of predictors in the D value model.

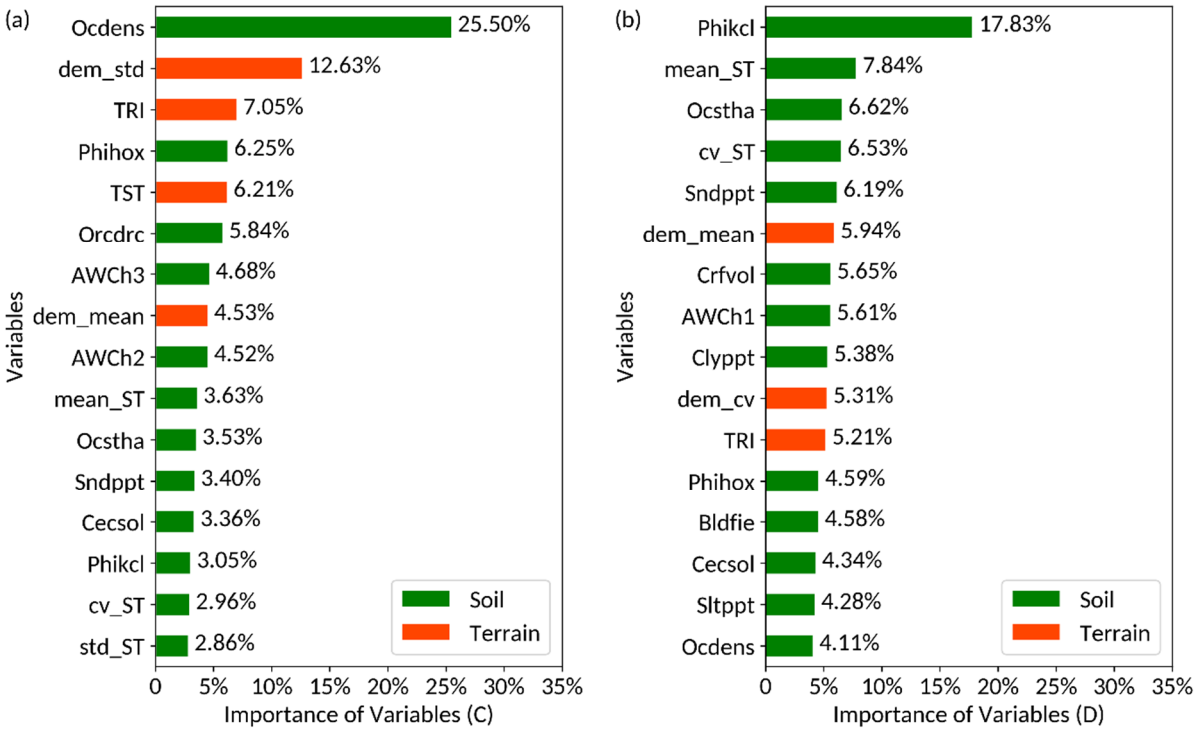


**Fig. 4.** Importance of the selected variables in the RF model for predicting the (a) C value and (b) D value.

### *4.1.3 Performance of RF model and calibration results of C and D*

A 10-fold cross-validation was used to evaluate the performance of the two RF models. Scatterplots between the true value and predicted value from the trained models are shown in Fig. 5. Both models performed quite well and the model for the C value obtained better scores ($R^2$ = 0.86, RMSE = 1.31 dB) than the one for the D value ($R^2$ = 0.61, RMSE = 2.38 dB/ $m^3 \cdot m^{-3}$). From Fig. 5, we can note an overestimation in the lower values and an underestimation in the higher values for both the C and D models, and the underestimation being stronger in the D value model. This underestimation is most likely caused by the training dataset that does not have enough pixels in the range of 20-25 dB/ $m^3 \cdot m^{-3}$. According to the statistics in the D values (Fig. 5(b)), the number of pixels used to train the model in that range (20-25 dB / $m^3 \cdot m^{-3}$) is around 20, accounting for only 1.58 % of the total number of training pixels.

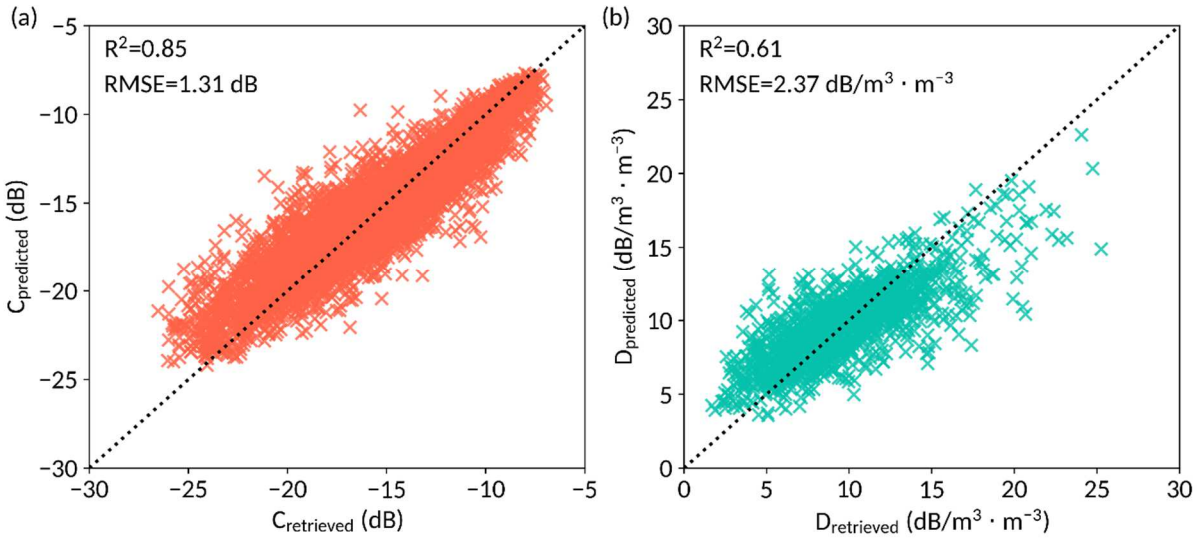


460

461 **Fig. 5.** Scatterplots between the retrieved and RF predicted values based on the 10 folders cross-
462 validation for the (a) C value and (b) D value.

463 The RF predicted maps for C and D in Africa are presented in Fig. 6 (a) and (b). To better
464 understand the spatial distribution of the C and D values in those two maps, we grouped the C
465 and D values in each IGBP vegetation type (Fig. 6 (c)). Fig. 6 (d) shows that the median of the
466 C values is similar (~ -14.8 dB) for each IGBP vegetation type. Very large variability in the C
467 values can be noted for barren or sparsely vegetated (BSV). When analyzing the Ocdens and
468 TRI data for BSV, we found that the pixels with the higher TRI values correspond to higher C
469 values, and the higher Ocdens values correspond to the lower C value. To a more limited extent,
470 the same results were obtained too for open shrubland (OSH), mostly in southern and northwest
471 Africa. With regard to the spatial distribution of the D values, OSH presents the lower values
472 in the map. As for the D values, the range of the D values is the largest for BSV among all
473 vegetation types. A large range in the D values is also obtained for cropland and grassland.

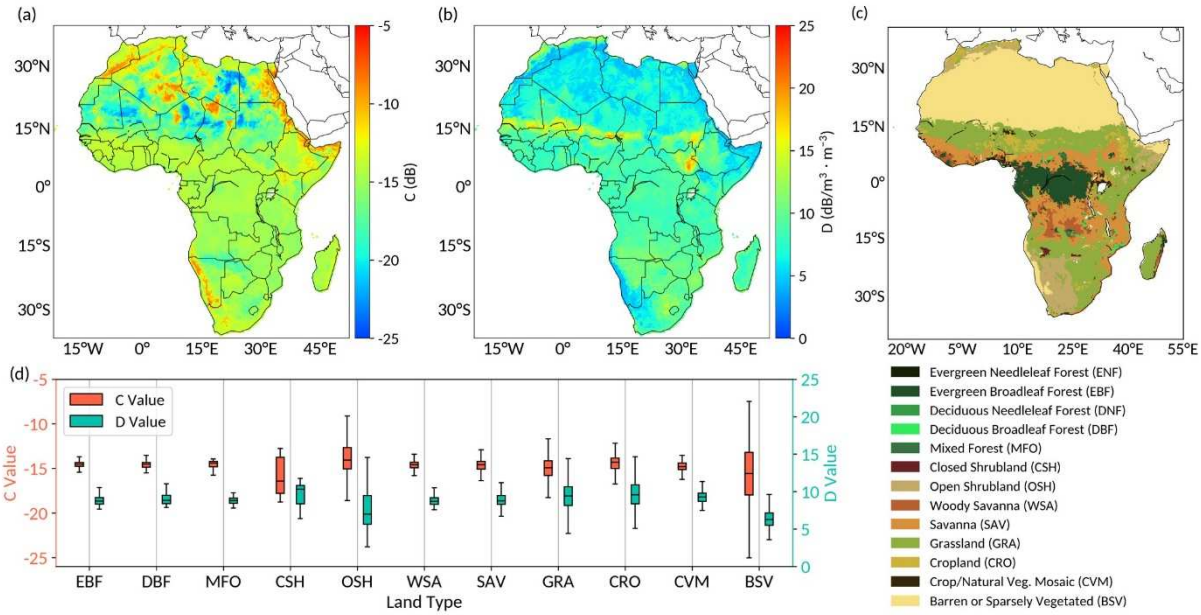


**Fig. 6.** Map of the (a) C and (b) D soil model parameters and (d) the corresponding boxplot in (c) different land cover types.

## 4.2 Calibration results of the vegetation parameter

To map the vegetation parameter A of the WCM model over Africa, we first computed the $A_0(i,j)$ values using Eq. (8) over the very dense vegetation (VDV) area for each day (t) and then calculated the mean value over all VDV pixels ($A_0(t)$) and the 95$^{th}$ percentile ($A_0^{95\%}(t)$). Fig 7 (a) shows the spatial distribution of the VDV areas. The VDV areas are mainly located in the Congo basin where the dominant land cover type is the evergreen broadleaf forests (Fig. 6 (c)). In this study, the vegetation calibration was made over five years (2015-2019). $A_0(t)$ presents lower values in winter and spring while larger values were found in summer when the vegetation growth reaches its peak (Fig 7 (b)). $A_0^{95\%}(t)$ has the same trend as $A_0(t)$ but with larger values. To calibrate the A value in WCM, we used $A_0(t)$ in most regions of Africa, and $A_0^{95\%}(t)$ was mainly adopted in the VDV areas (Fig 7 (c)).

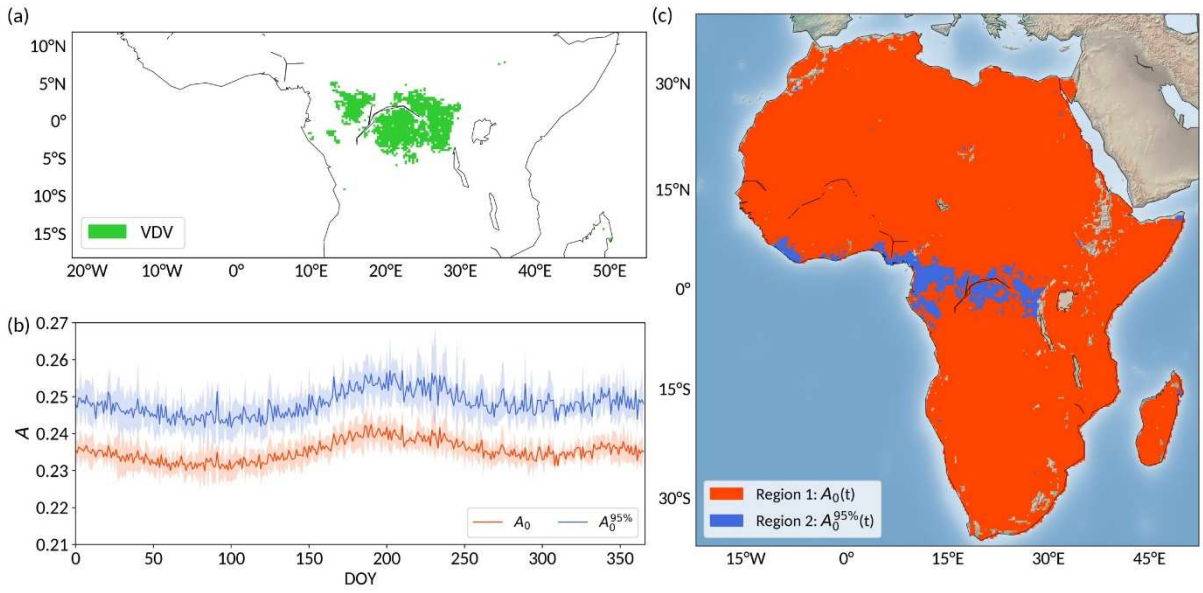


**Fig. 7.** (a) Map of the very dense vegetation (VDV) region selected in this study, and (b) daily values of $A_0$ and $A_0^{95\%}$ for five years (2015-2019). The solid line represents the average value of five years, and the shading describes one standard deviation. (c) Map of Region 1 and Region 2 used in the calibration of the vegetation parameter.

## 4.3 Evaluation of IB VOD

The performance of IB VOD was evaluated in both space and time. The spatial correlation between IB VOD and AGB (Saatchi AGB, CCI AGB), TH (Simard TH, Patapov TH) and the temporal correlation between IB VOD and VIs (NDVI, EVI and LAI) were computed as performance metrics. In addition, three other VOD datasets (ASCAT V16, AMSR2 LPRM V5 and VODCA LPRM V6) retrieved at the same frequency band (C-band) were also included in the inter-comparison. As VODCA LPRM V6 VOD data was only updated until the year 2018, the temporal performance of IB VOD was evaluated from 2015 to 2018.

### *4.3.1 Spatial patterns of IB VOD*

Fig. 8 shows the average value of IB VOD and three other VODs (ASCAT V16, AMSR2 LPRM V5 and VODCA LPRM V6) computed from 2015 to 2018. All maps present similar general

spatial patterns: the highest VOD values are distributed in the equatorial rain forests and the lowest values in the Sahara Desert. The VOD values generally decrease as the distance from the equator increases. In terms of VOD range, IB VOD has a larger range of values (~ 0 - 1.5) than the three other VOD. The changing patterns with the latitude of IB VOD are more consistent with those of V16 VOD which is computed from the same sensor (ASCAT) (Fig. 8 (d)). There are also some differences between IB VOD and the three other VOD. The values of IB VOD in the rainforests are ~ 1.5 times larger than those of VODCA LPRM V6 VOD. Zonal VOD averages show that the peak of IB VOD is sharper and presents a faster decrease with the increasing distance to the equator than AMSR2 LPRM V5 and VODCA LPRM V6 VOD (Fig. 8 (d)). Moreover, the values of IB VOD are generally lower than those of the three other VOD datasets except for the rainforest region (Fig. 8 (d)). Importantly, IB VOD shows a very similar pattern with CCI AGB and Tree height (Fig. 8 (d) & (h)).

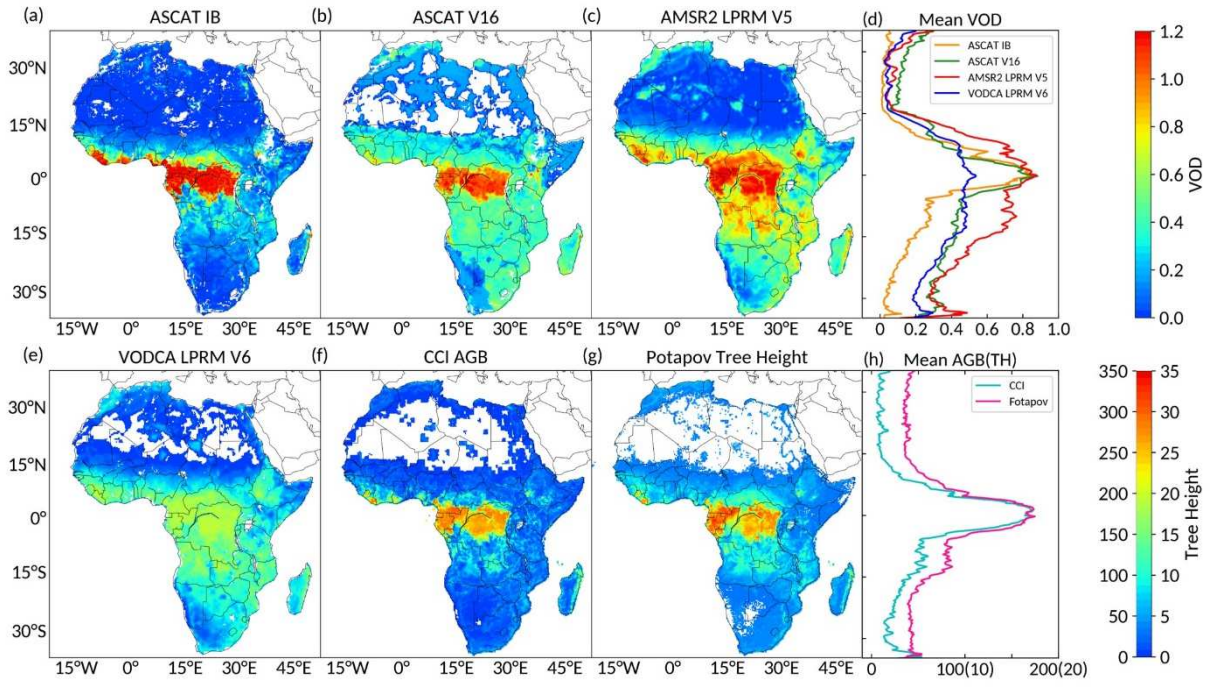


**Fig. 8.** Temporal average of VOD for (a) ASCAT IB, (b) ASCAT V16, (c) AMSR2 LPRM V5 and (e) VODCA LPRM V6 from years 2015-2018, and (f) CCI AGB and (g) Potapov tree height. Side plots show the zonal average for (d) the four VOD and (h) CCI AGB and Potapov TH data sets.

Boxplots of the four VOD for each land cover class are presented in Fig. 9 (a). Wide quantile ranges are found for IB VOD over the region covered by evergreen broadleaf forest (EBF), woody savanna (WSA) and cropland/natural vegetation mosaic (CVM). The same can also be noted for ASCAT V16 and AMSR2 LPRM V5 VOD for the EBF and CVW classes, respectively, but to a lower extent. VODCA LPRM V6 VOD has a very narrow range in each vegetated IGBP class and particularly in EBF. The highest yearly VOD values were obtained for EBF, followed by WSA, MFO and DBF (Fig. 9 (b)). Except for EBF, WSA and CVM, the lowest average value was obtained with IB VOD over each land cover class. The change in IB VOD for the different vegetation classes is quite consistent with that of AGB (R=0.94-0.95), while the consistency is less clear for the three other VOD datasets. For example, the AGB value of EBF is four times larger than that of DBF, while the change in the AMSR2 LPRM V5 and VODCA LPRM V6 VOD values for these two vegetation classes is much lower.

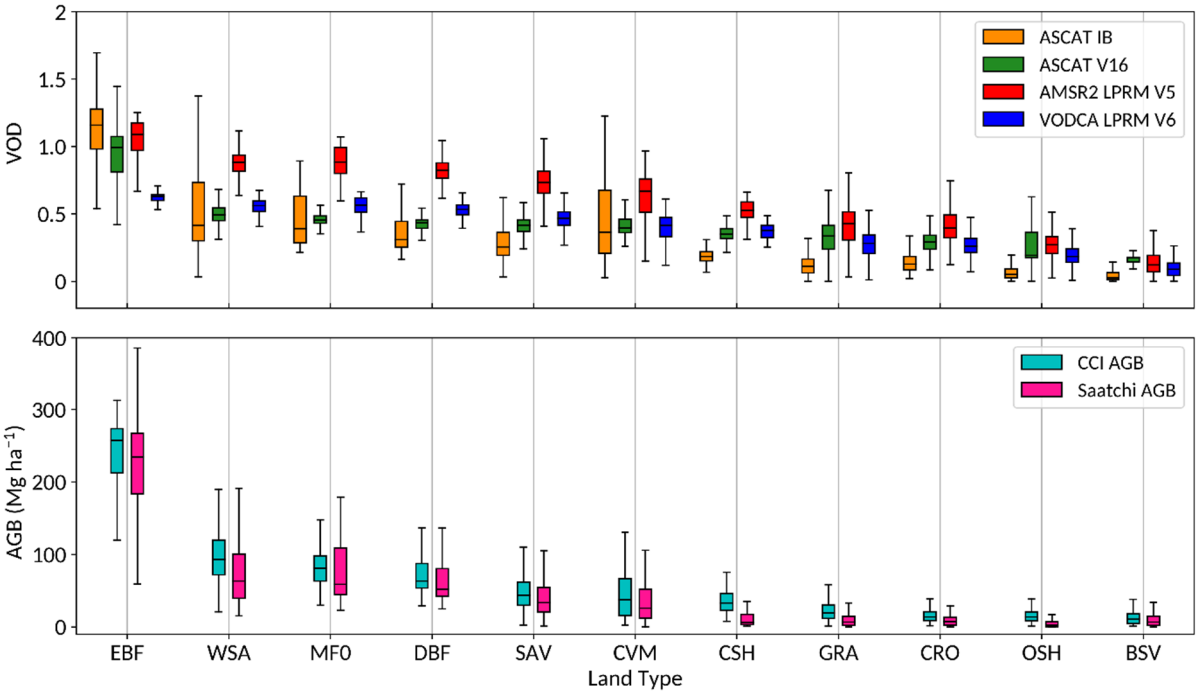


**Fig. 9.** Boxplots of the four VOD datasets (ASCAT IB, ASCAT V16, AMSR2 LPRM V5, and VODCA LPRM V6) (top) and two AGB datasets (CCI and Saatchi) (bottom) for different IGBP land cover classes.

### *4.3.2 Evaluating IB VOD against aboveground biomass and tree height*

When considering the spatial relationship between the four yearly average VOD and AGB (Fig. 10), it was found to be almost linear for the active VOD datasets (IB and V16) and quite non-linear (exponential form) for the passive ones. In terms of linear fit, highest spatial correlation values were obtained with IB VOD (R = 0.92), followed by V16 VOD (R = 0.83-0.86), AMSR2 LPRM V5 VOD (R = 0.76) and VODCA LPRM V6 VOD (R = 0.69). The spatial relationship between the two AGB and the four VOD datasets was computed for each land cover type (Table 2). The highest spatial correlation (R-value) with AGB was obtained with IB VOD in most of the vegetation types, except for evergreen broadleaf forest (EBF) and cropland (CRO). For EBF, CRO and barren or sparsely vegetated (BSV), the highest R-values were obtained with ASCAT V16 and AMSR2/VODCA VOD, respectively.

In order to assess the capacity of VOD to predict AGB, two functions (linear and exponential regression) were selected to compute the best-fitted relationships for each VOD dataset. The R correlation coefficient calculated between predicted and reference AGB is used to evaluate the quality of the prediction. In terms of predicted AGB, the highest R values (R = 0.92) were obtained by IB VOD, followed by AMSR2 LPRM V5 VOD (R ~ 0.88-0.90) while lower R values were obtained for VODCA LPRM V6 and ASCAT V16 VOD (R ~ 0.83-0.86)

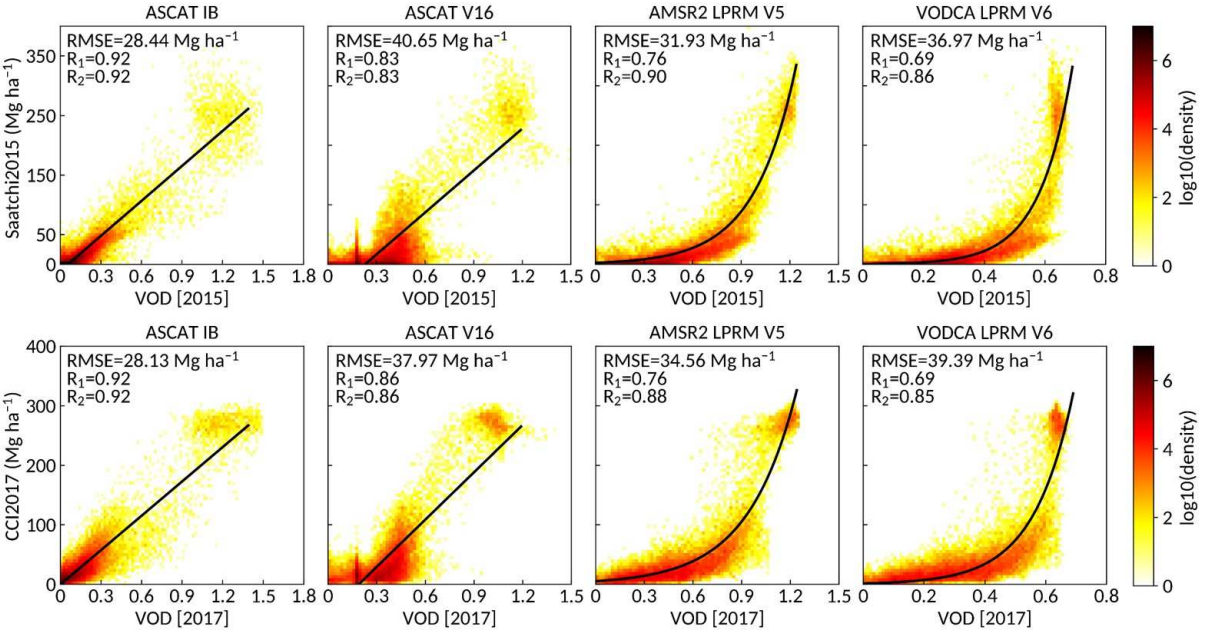


**Fig.10.** Density scatter plots showing the spatial relationship between the four yearly average VOD datasets (from left to right: ASCAT IB, ASCAT V16, AMSR2 LPRM V5, VODCA LPRM V6) and two AGB datasets (from top to bottom: Saatchi, CCI). $R_1$ represents the spatial correlation between VOD and reference AGB, while $R_2$ represents the spatial correlation between predicted AGB and reference AGB. Computations were made over 2015 -2017. The solid line is the fitted line.

**Table 2.** Spatial correlation of the four VOD datasets with the two CCI and Saatchi AGB datasets for different IGBP land cover classes.

| AGB Product | VOD Product | EBF | DBF | MFO | CSH | OSH | WSA | SAV | GRO | CRO | CVM | BSV | R_total |
|---|---|---|---|---|---|---|---|---|---|---|---|---|---|
| Saatchi 2015 | ASCAT IB | 0.54 | **0.83** | **0.88** | **0.62** | **0.30** | **0.78** | **0.78** | **0.58** | 0.58 | **0.79** | **0.21** | **0.92** |
| | ASCAT V16 | **0.58** | -0.22 | -0.26 | -0.26 | -0.16 | 0.67 | 0.31 | 0.17 | 0.17 | 0.30 | 0.11 | 0.83 |
| | AMSR2 LPRM V5 | 0.54 | 0.53 | 0.74 | 0.23 | 0.09 | 0.31 | 0.61 | 0.51 | **0.62** | 0.57 | 0.19 | 0.76 |
| | VODCA LPRM V6 | 0.36 | 0.40 | 0.62 | -0.20 | - | 0.18 | 0.57 | 0.44 | 0.59 | 0.56 | 0.18 | 0.69 |
| CCI 2017 | ASCAT IB | 0.70 | **0.31** | - | **0.66** | **0.27** | **0.71** | **0.60** | **0.53** | 0.36 | **0.72** | 0.28 | **0.92** |
| | ASCAT V16 | **0.74** | - | **0.47** | - | -0.08 | 0.64 | 0.43 | 0.30 | 0.20 | 0.45 | 0.09 | 0.86 |
| | AMSR2 LPRM V5 | 0.55 | 0.30 | - | - | 0.12 | 0.32 | 0.38 | 0.45 | **0.39** | 0.57 | **0.40** | 0.76 |
| | VODCA LPRM V6 | 0.38 | 0.21 | - | -0.32 | 0.05 | 0.18 | 0.33 | 0.40 | 0.36 | 0.55 | 0.37 | 0.69 |

Note: [-] indicates that correlation is not significant (p-value>0.05). The number of pixels used in the computation are 2734 (EBF), 200 (DBF), 180 (MF), 118 (CS), 1746 (OS), 1237 (WS), 5628 (S), 8636 (G), 1269 (C), 238 (CNVM), 1623 (BSV).

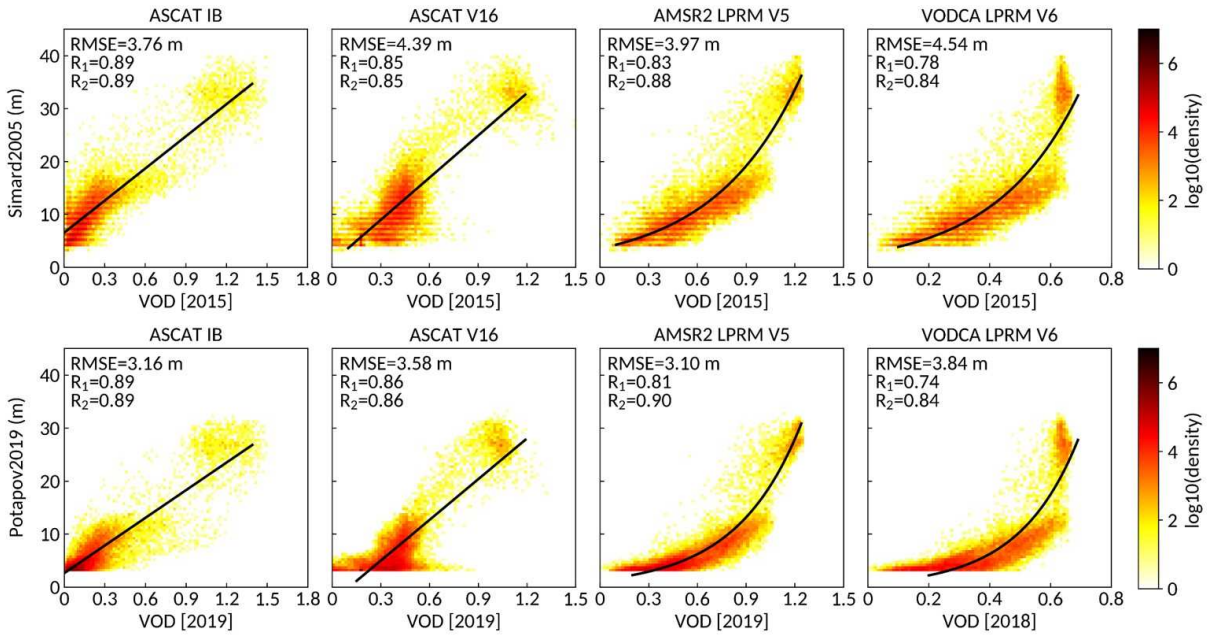


**Fig.11.** Density scatter plots showing the spatial relationship between the four yearly average VOD datasets (from left to right: ASCAT IB, ASCAT V16, AMSR2 LPRM V5 and VODCA LPRM V6) and two tree height datasets (from top to bottom: Simard, Patapov). $R_1$ represents the spatial correlation between VOD and tree height (TH), while $R_2$ represents the relationship between predicted TH and reference TH. The solid line is the fitted line.

Fig. 11 shows the density scatter plot between two tree height (TH) datasets (Simard and Patapov) and the four VOD datasets. The active VOD datasets have a more pronounced linear spatial relationship with the two TH datasets than the passive VOD, similarly with the result obtained for AGB. IB VOD presents the best spatial linear relationship with the two TH datasets (R ~ 0.89). In contrast, VODCA LPRM V6 VOD got the lowest R-value (R = 0.74-0.78). Regarding the potential to predict TH, VODCA LPRM V6 VOD also showed the poorest performances as saturation happened for high VOD values. The best ability to predict TH for both the Simard and Potapov datasets was obtained by IB and AMSR2 LPRM V5 VOD (R~ 0.89-0.90).

### *4.3.3 Evaluating IB VOD against MODIS VIs*

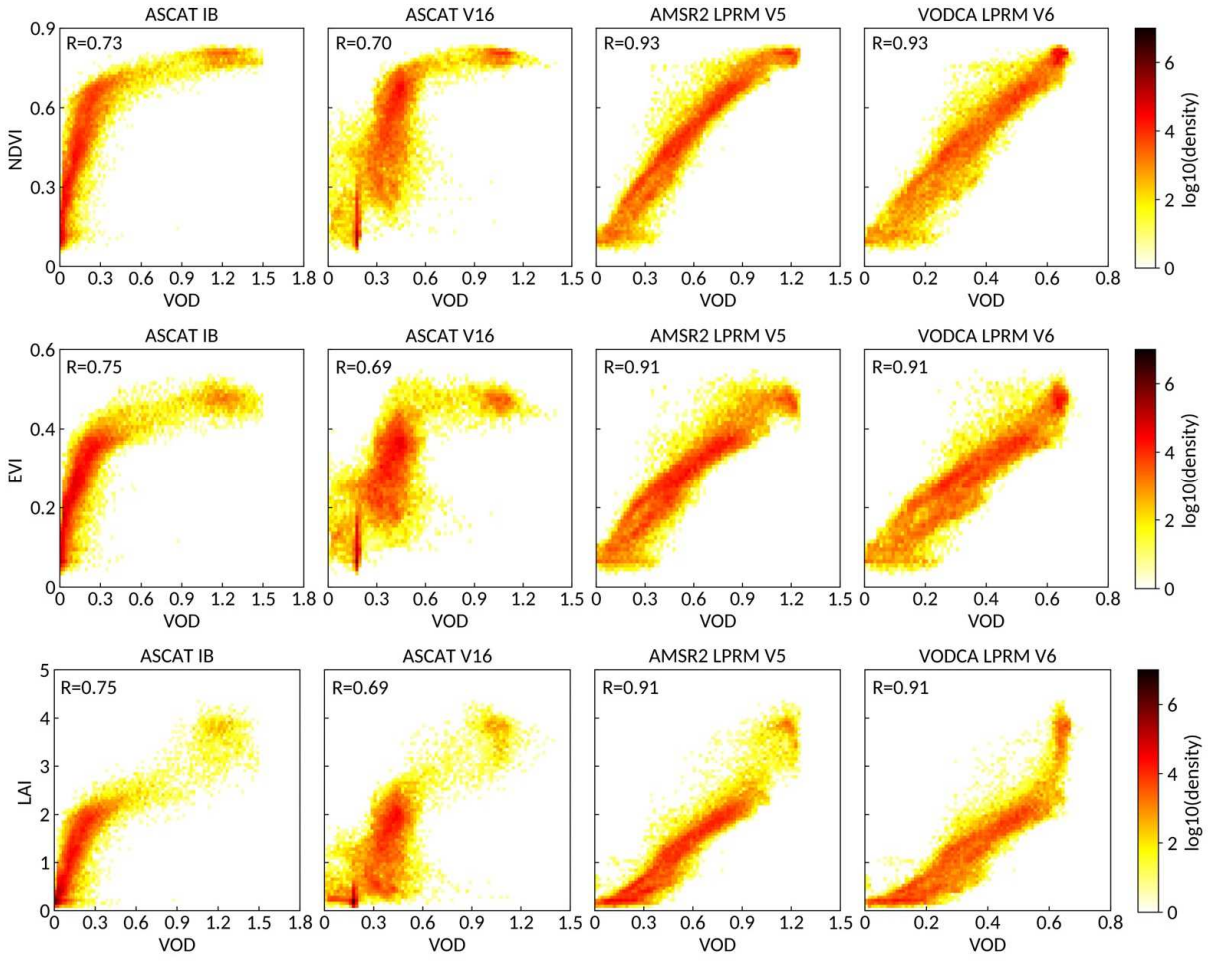


**Fig.12.** Density scatter plots of the spatial relationship between four yearly average VOD datasets (from left to right: IB, ASCAT V16, AMSR2 LPRM V5 and VODCA LPRM V6) and two MODIS VI datasets (from top to bottom: NDVI, EVI and LAI).

With respect to the spatial relationship between the VOD and MODIS VIs, Fig. 12 shows saturation for high VIs values is more obvious for the active VOD datasets (ASCAT IB and V16), while the relationship is almost linear for the passive VOD (AMSR2 LPRM V5 and VODCA LPRM V6). Saturation starts when the values of NDVI (EVI, LAI) exceeds ~ 0.7(0.4, 2). The correlation coefficients obtained with the active VOD dataset are lower than 0.75. Higher spatial correlations (R ~ 0.91-0.93) were obtained with passive VOD, but saturation can

591 also be noted for AMSR2 LPRM V5 for higher NDVI and EVI values and VODCA LPRM V6
592 for higher LAI values.
593 In order to evaluate the ability of IB VOD to monitor the vegetation dynamics, the temporal
594 correlations between 16-day average VOD and MODIS VIs (NDVI, EVI and LAI) were
595 computed for each pixel from 2015 to 2018 (Fig.13). IB VOD presents a positive temporal
596 correlation with each VI in most regions of the African continent (values exceeding 0.85 in
597 Nigeria for instance). Negative correlation values (R∼-0.7) can be noted in some arid and semi-
598 arid regions, such as the south of Ethiopia and western Namibia. Compared with the results of
599 the three other VOD datasets, we found that the spatial distribution of pixels with a positive
600 correlation obtained with IB VOD is similar to that obtained with AMSR2 LPRM V5 and
601 VODCA LPRM V6 VOD. Although ASCAT V16 VOD shows generally different spatial
602 patterns (Fig 13 (b), (f) and (g)), similar negative correlation values were found in South Africa
603 and the Sahara Desert. Interestingly, for some pixels in the north of Africa, the temporal
604 correlation between each VI and passive VOD is opposite to that obtained with the active VOD.
605 A more detailed analysis of these results as a function of land cover classes is given in
606 Supplementary.

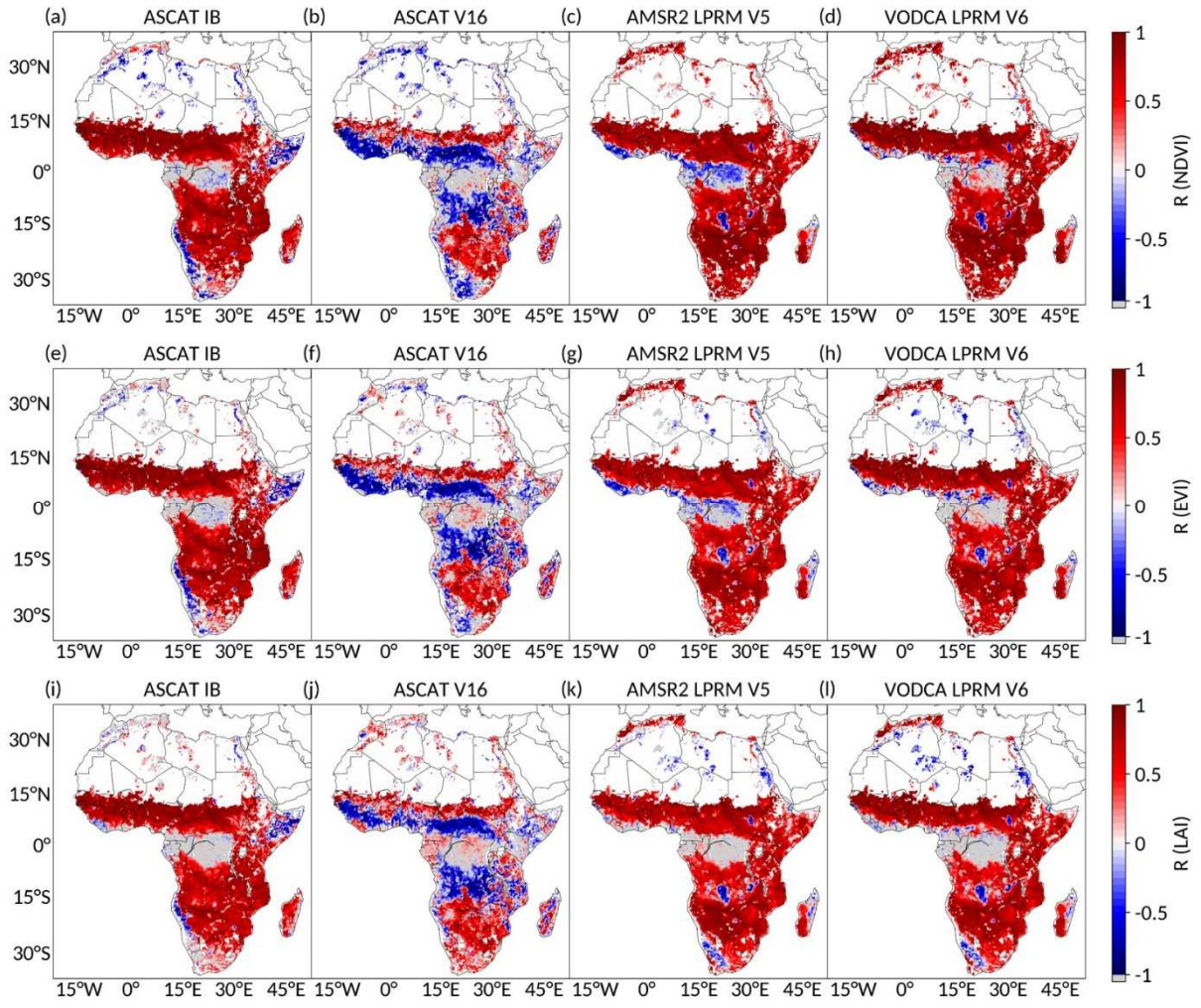


607

608 **Fig.13.** Temporal correlations between four VOD datasets (from left to right: ASCAT IB,
609 ASCAT V16, AMSR2 LPRM V5 and VODCA LPRM V6) and three MODIS VIs datasets
610 (from top to bottom: NDVI, EVI and LAI) for each pixel from 2015 to 2018. Grey pixels
611 correspond to pixels where correlation is not significant ($p > 0.05$). Blank pixels denote "no
612 valid data".

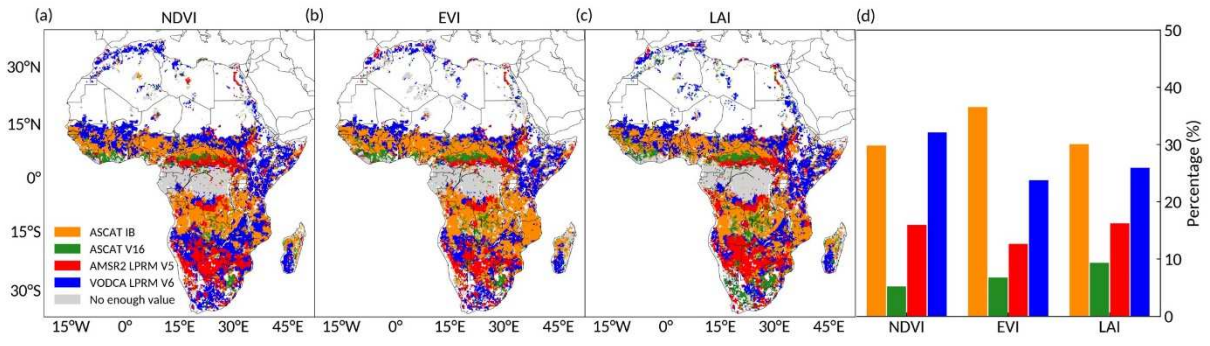


613

**Fig.14.** Maps showing which VOD datasets obtained the highest absolute temporal correlation (R) values with MODIS VIs and (d) its percentage of coverage. Grey pixels correspond to pixels where the correlation is not significant ($p > 0.05$). Blank pixels denote "no valid data".

To get an easier overview of the performance of each VOD dataset in terms of temporal correlation, a map showing which VOD products showed the highest temporal correlation with MODIS VIs over Africa is given in Fig. 14. For IB, the pixels with the highest temporal correlations with NDVI are mainly distributed in the centre-west (3°S-15°S). ASCAT V16 obtained the highest correlation values in a few regions in Centre Africa. The highest correlation values for AMSR2 LPRM V5 VOD were located in the south of Africa and the north of the Congo basin. For VODCA LPRM V6 VOD, the distribution of the highest correlation values is scattered all over Africa, mainly out of the central regions of Africa. Similar results were also found for EVI and LAI. As noted above, more pixels obtained the highest correlation values with EVI and LAI for IB VOD, especially in eastern Africa (Tanzania) and south of the Sahel region.

Fig. 14 (c) gives the percentage of pixels where the highest correlation was obtained for each VOD product. IB VOD shows the best performance with EVI (LAI), over 36.65 % (30.19 %) of the pixels, followed by VODCA LPRM V6 VOD (23.87 % for EVI, 26.06 % for LAI). Conversely, regarding NDVI, VODCA LPRM V6 VOD obtained the best score (32.25 %), followed by IB (29.94 %). The lowest scores were obtained by ASCAT V16 VOD (5.32 % for NDVI, 6.88 % for EVI). In addition, we plotted the pixels with high correlation differences (HCD) in Fig. S1 to evaluate if there is a strong difference between the products obtaining the best scores. HCD means that the highest correlation value with one product is larger by 0.1 than that obtained with all the other products. Overall, IB obtained the best score in terms of temporal

correlation in many pixels and this score was strongly (by a value of 0.1) improved in comparison with the other products.

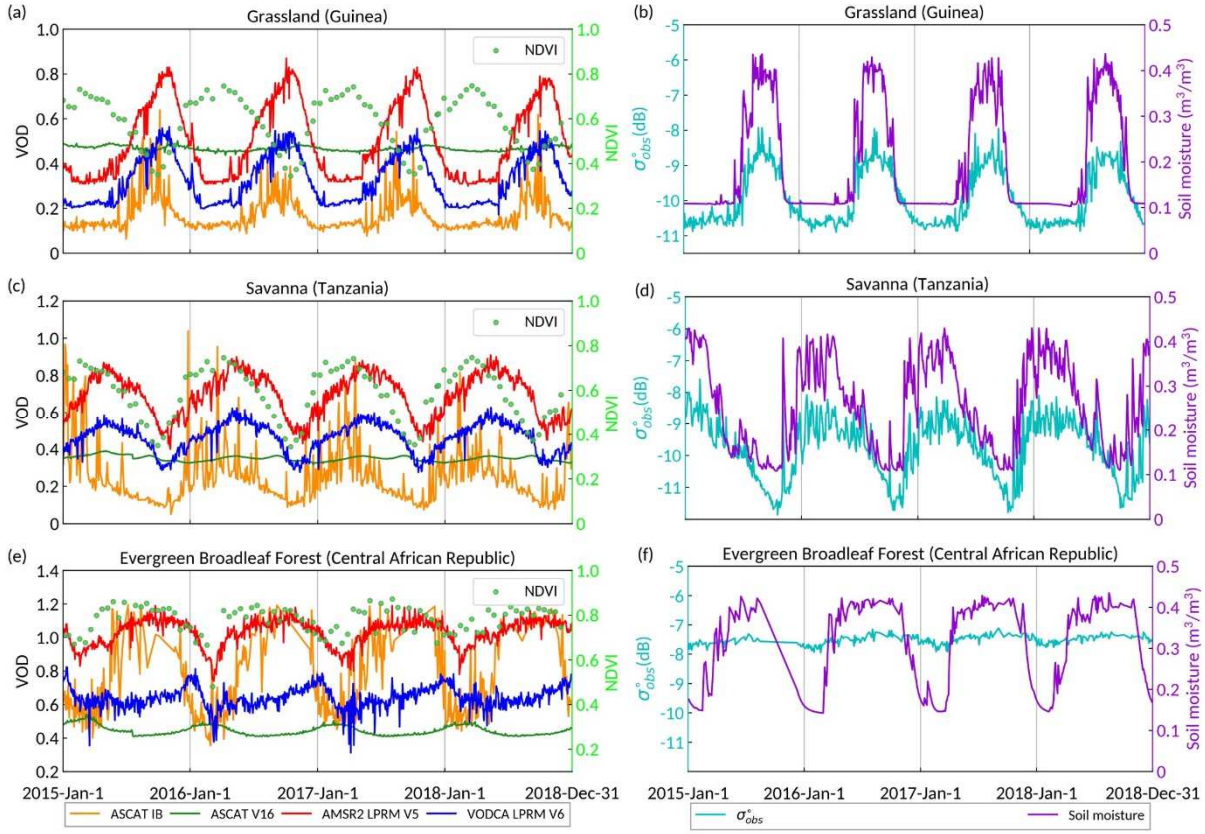


**Fig. 15.** Time series of the four VOD products (daily), NDVI, ASCAT backscatter and ERA5-Land Soil moisture from January 2015 to December 2018 over three types of vegetation (Grassland, Savanna and Evergreen Broadleaf Forest).

The seasonal dynamics of IB and three other VOD are also analysed based on the daily time series of VOD along with NDVI at three selected sites (Fig. 15). ASCAT IB VOD is noisier at a daily time-scale than the three other VOD products (this aspect will be explored in discussion), while a clear seasonal change can be well observed for all VOD products. AMSR2 LPRM V5 and VODCA LPRM V6 VOD present similar seasonal variations but with different values. This is because VODCA LPRM V6 VOD is a fusion of VOD retrieval results from multiple sensors. The VODCA data used in this study were retrieved from AMSR2 and then calibrated via cumulative distribution function matching using AMSR-E as the scaling reference (Moesinger

et al., 2020). ASCAT V16 VOD is more stable (almost flat) than the three other VOD products (green line in Fig.15 (a), (c) and (e)). This could be explained by the fact that V16 VOD is derived using two coefficients (slope and curvature) of the second-order Taylor expansion (Teubner et al., 2019), and those two coefficients are averaged by using a kernel smoother with a half-width window of 21 days (Vreugdenhil et al., 2020). The value of V16 VOD decreases with the increase of NDVI (Fig. 14 (e)), which can explain why a negative temporal correlation between V16 VOD with NDVI and EVI was found over some areas of evergreen broadleaf forests (Fig 15. (b) and (f)). At the same time, a large time lag (~180 days) between the four VOD products and NDVI (Fig. 15 (a)) was found in grassland. Tian et al. (2018) and Lawrence et al. (2014) also found time lags, varying by a large range of days, between L-VOD and NDVI over different vegetation types.

# 5. Discussion

The evaluation and inter-comparison results presented in this study show that IB VOD obtained good scores in both temporal and spatial terms. This promising result indicates that IB VOD is a valid and alternative candidate for application in biomass and carbon estimation. We should also notice that there are some uncertainties in IB VOD. Those uncertainties mainly come from the soil and vegetation model calibration and SM input.

As for the soil parameter calibration, we calculated the value of C and D for each pixel corresponding to bare land without any vegetation cover throughout the year (case 1) and land covered by a certain degree of sparse dynamic vegetation (case 2), which is different from previous studies where the soil coefficients (C and D) of the Ulaby linear model were calibrated from experimental data measured over different sites. Then the calibration of C and D was extended at continent-scale using a RF machine learning method. Compared with the C and D values computed in Shamambo et al. (2019), the values of C and D obtained in our study are

677 lower and their range is larger. Although Shamambo et al. (2019) also used ASCAT data, their
678 different research region (south-west of France) and calibration methods caused different
679 results. For the D value, numerous experimental studies at C-band have shown a variable
680 sensitivity of the radar signal to soil moisture, varying approximately between 5 dB / $m^3 \cdot m^{-3}$
681 and 30 dB / $m^3 \cdot m^{-3}$ (Baghdadi et al., 2008; Baghdadi et al., 2016; Verhoest et al., 2008). Our
682 results are in good agreement with these previous results. Fig 6 (a) shows very low C values on
683 smooth dunes (in Sahara) and the strongest values on areas with topography (including in the
684 Sahara), which is in very good coherence with the reality of the terrain and the nature of the
685 scattering in these areas. However, we should note that the performance of the RF model used
686 to estimate the soil parameters is better for C than for D (Fig. 5). One of the reasons could be
687 that the number of pixels used to train the D value model is far less than that used to train the
688 C value model (1262 pixels for C *vs* 8786 pixels for D). Moreover, pixels with a low R-value
689 (<0.4) (accounting for around 8 % of the data in category 1, Fig. S2) will also affect the training
690 of the model. In the future, to improve the C and D model performance, the calibration will be
691 carried at a larger scale and the threshold of the R-value will be increased to select "better"
692 pixels.

693 As for the vegetation parameter (A) calibration, its value was set to a spatially constant value
694 in only two regions of Africa for each day. Ma et al. (2020) found that changes in the value of
695 A have little effect on the simulation of the VV polarized backscatter when the vegetation water
696 content is lower than 1.5 $kg/m^2$. In addition, the A parameter is related to the vegetation single
697 scattering albedo (ω) which is a key parameter in the passive microwave VOD retrievals. In the
698 LPDR and LPRM algorithms, ω was set to a constant value globally (Du et al., 2017; Owe et
699 al., 2001). However, studies in the passive microwave domain have recently suggested that the
700 vegetation single scattering albedo may vary seasonally in different vegetation types (Baur et
701 al. 2019). Bindlish and Barros (2001) also found that better performances in SM retrievals were

obtained with the WCM model when different A values were set for different types of land cover. Therefore, IGBP-based or pixel-based calibration of A could be considered in future works. Moreover, the daily A value was calibrated over VDV in Africa and then extended to the whole of Africa. When we will extend our method to a global scale, the calibration of the A value should thus be re-evaluated. In addition, Shamambo et al. (2019) found that the correlation between the observed backscatter and WCM simulated backscatter is small or negative in karstic areas. This information should also be considered in future analyses.

Our retrieval algorithm used the ERA5-Land SM as a known SM input of the retrieval algorithm. Therefore, the IB VOD retrievals made in this study may be sensitive to the quality of the ERA5-Land SM dataset. A simple sensitivity analysis was made to assess the effect of the uncertainty in SM on the retrieved VOD values. Fig. S3 shows that decreasing (increasing) SM by a value of 0.05 $m^3/m^3$ (that corresponds to an estimate of the ubRMSE of ERA5-Land (Chen et al., 2021)) will lead to a decrease (increase) in VOD of 0.02 over grassland, 0.01 over savanna, and 0.02 over the evergreen broadleaf forest. The relative change of VOD in grassland is 16.21 % which is larger than that in savanna (5.24 %) and evergreen broadleaf forest (2.57 %). This is because the observed backscatter is dominated by soil scattering for low vegetation, so that the uncertainty in SM has a larger influence on the retrieval of VOD in grassland. Anyway, the relative change of VOD, due to the uncertainty in input SM, may appear as relatively modest if we consider the uncertainties existing in global AGB maps, which may differ by about 50% in some regions. Moreover, when they will become available, any other more appropriate soil moisture data set could be used in the retrieval based on the framework proposed in this study.

IB VOD was directly computed from the observed values of the ASCAT backscatter ( $\sigma^{\circ}_{obs}$ ) and the ERA5-Land SM, so that large daily fluctuations of SM and $\sigma^{\circ}_{obs}$ made IB VOD noisier than the three other VOD products (Fig. 15 (e), (f) and (g)). Although IB VOD is noisy, it still shows

obvious seasonal dynamics. There are also some possible ways to improve the time series of the daily IB VOD values in the future. For instance, in the LPDR algorithm (Du et al., 2017), a 30-day moving median filter was applied to the daily X-band VOD (Du et al., 2017), which makes the time series of LPDR X-band VOD very smooth. This filtering step could be used in the future as it helps to improve the temporal continuity of VOD and reduce short-term noises (for illustration, in Fig. S4, a moving window was applied to all VOD time series shown in Fig. 15). Another possible way is to use the ASCAT multi-angle data: the normalized ASCAT backscatter at the incidence angle $\theta = 40$ degrees can be converted to the backscatter at any angle by using a second-order Taylor expansion that describes the angular backscatter dependency (Hahn et al., 2017). More information originating from different angles could be added to the retrieval algorithm to improve the IB VOD performance. However, this will make the calibration more complex. All these different results show the importance of improving the time-series of daily IB VOD in future works.

In this study, IB VOD is spatially linearly related to AGB and TH. The relationships with VIs exhibit a saturation for high IB VOD values (Fig. 10-12). In contrast, passive VOD shows a linear relationship with VIs but shows saturation for high AGB and TH values. This is can be explained by the fact the active microwave data are generally more sensitive to vegetation structure compared with passive data (Ferrazzoli et al., 1989; Fung and Eom, 1985; Wigneron et al., 1999). Active microwave radiations are affected by a two-way attenuation through the canopy layer, while, in the passive domain, there is one-way attenuation (Fernandez-Moran et al., 2017). C-band radar backscatter return from the middle of vegetation (between canopy top and ground) (Pulliainen et al., 1994), therefore VOD retrieved from ASCAT could more sensitive to branch and trunk diameter which are well correlated to biomass (Mankou et al., 2021), explaining the good correlation between ASCAT VOD and AGB. Conversely, as VIs were calculated from optical sensors they are more sensitive to saturation. The high sensitivity

751 of ASCAT VOD to AGB is a new and interesting finding of this study which should be
752 investigated further.

## 753 6. Conclusion and outlook

754 An alternative ASCAT-IB VOD product was retrieved in this study during 2015-2019 over
755 Africa by using the water cloud model coupled with the Ulaby linear model. The idea of using
756 the soil moisture as input was adopted in the retrievals of VOD. Two Random Forest models
757 were trained to map the soil parameters (C and D) of the Ulaby linear model, and the trained
758 model showed good performance ($R^2$=0.85 for C and $R^2$=0.61 for D). For the vegetation
759 parameter (A) of WCM, a temporally dynamic value calibrated from observations over the very
760 dense vegetated area was used. IB VOD and the three other VOD products were evaluated
761 against several vegetation datasets (AGB, tree height and MODIS VIs). Comparison with other
762 VOD products suggested IB VOD has advantages in terms of both spatial and temporal
763 performances. Especially, IB VOD presents a very good linear relationship with AGB and tree
764 height data (R ~ 0.89-0.92) showing the considerable potential of IB VOD to study global AGB
765 and tree height changes. Moreover, the temporal correlation between IB VOD and NDVI or
766 EVI showed obvious improvements (> 0.1) in savanna and woody savanna compared to the
767 three other VOD products considered in the present study.

768 The encouraging results found in Africa suggest that we can extend the proposed method to
769 produce a long term (from 2007- present) and global IB VOD product. In addition, Steele-
770 Dunne et al. (2012) and Frolking et al. (2011) found that variations in canopy water content
771 could account for the backscatter variations between the ascending and descending orbits.
772 Therefore, IB VOD retrieved from different orbits can be explored in the future to analyse daily
773 changes in the vegetation water content. Moreover, when soil moisture datasets at a finer spatial
774 resolution downscaled from several sensors will be available (Fan et al., 2015) and swarms of
775 SAR cubesats will be available in a decade, the method used in the present study could be

extended to retrieve a high-resolution active VOD product (e.g. from Sentinel-1). More importantly, IB VOD is independent of passive microwave observations, and as such, it could be used in inter-comparison of VOD products based on the triple collocation (TC) or TC-related methods (Li et al., 2021). Moreover, two independently (passive & active) retrieved VOD products could be used in a physics-based VOD model (Jackson and Schmugge, 1991) to decouple the effects of the vegetation moisture content / structure / biomass on the microwave observations.

## Data availability

ASCAT IB VOD was developed by INRAE (Institut national de recherche pour l'agriculture, l'alimentation et l'environnement). ASCAT IB VOD will be made available at the INRAE Bordeaux remote sensing lab website (https://ib.remote-sensing.inrae.fr/).

## Acknowledgments

This work is conducted under the support of CNES, France (Centre National d'Etudes Spatiales) within the TOSCA (Terre Ocean Surface Continentales Atmosphère) program. The authors would like to thank EUMETSAT for providing the ASCAT data, LAADS DAAS for providing the MODIS data, and ISRIC providing the SoilGird250m data. Xiangzhuo Liu was sponsored by China Scholarship Council (201906070167), and wished to thank one of his best friends, Gongfan Wang. The authors also wish to thank the three reviewers for their helpful suggestions/corrections on the original manuscript.

## Appendix A. Vegetation variables used for validation

### A.1 Aboveground biomass

Two static AGB benchmark maps were applied to assess the performance of IB VOD for monitoring the aboveground vegetation biomass. The first AGB map (referred to as Saatchi

AGB) was extracted from the 1 km resolution AGB dataset developed by Saatchi et al. (2011). We used the updated Saatchi AGB that is representative of AGB circa 2015 (Carreiras et al. 2017; Saatchi et al. 2011).

The second AGB map (Fig. 8 (f)) (referred to as CCI AGB) which has a spatial resolution of 100 m was extracted from the European Space Agency's (ESA's) Climate Change Initiative (CCI) AGB dataset (Santoro and Cartus 2019). This dataset was produced using 2017 data from the Synthetic Aperture Radar (SAR) C-band Sentinel-1 and L-band Advanced Land Observing Satellite (ALOS-2) Phased Array L-band SAR (PALSAR-2). More details about this AGB map can be referred to Santoro and Cartus (2019).

## A.2 Lidar tree height

Two kinds of tree height datasets were used to evaluate the IB VOD performance. The first dataset was developed by Simard et al. (2011) at 1-km resolution. It was generated using data collected in 2005 by the Geoscience Laser Altimeter System (GLAS) sensor. For the areas not directly covered by the lidar footprint, tree height was simulated with vegetation, topography and climatology data through Random Forest. The second dataset was a newly released product (Potapov et al. 2020) (Fig. 8 (g)). This 30 m resolution dataset was generated from Global Ecosystem Dynamics Investigation (GEDI) lidar measurements and the Landsat analysis-ready data (ARD) (Qiu et al. 2018) acquired in the year 2019.

## A.3 MODIS vegetation indices

Three MODIS vegetation indices (VIs), NDVI, EVI and LAI, were used to evaluate the temporal performance of IB VOD. NDVI and EVI were obtained from MODIS MOD13A1 version 6 product (Didan 2015) at a spatial resolution of 500 m and a temporal resolution of 16 days. LAI data were obtained from MCD15A2H (Myneni et al., 2015) at a spatial resolution of 500 m and a temporal resolution of 8 days. These MODIS VIs were used to test the IB VOD's

823 sensitivity to the green photosynthetic activity of vegetation in both space and time. NDVI is
824 derived from the near-infrared and red frequency bands and presents saturation in areas with
825 dense vegetation (Huete et al. 2002). Compared to NDVI, EVI is less prone to saturation as a
826 band in the blue frequency was added in the calculation of the indices. Only VIs observations
827 with the corresponding flag set to "good quality" were used. We then adopted an arithmetic
828 averaging method to resample these two vegetation indices to the same projection with a spatial
829 resolution of 0.25 degree.

830

# Appendix Table

**Appendix Table 1**. Soil property data used to calibrate the soil model parameters

| ID | Name | Description | Units |
|---|---|---|---|
| 1 | AWCh1 | Available soil water capacity (volumetric fraction) with FC = pF 2.0 | % |
| 2 | AWCh2 | Available soil water capacity (volumetric fraction) with FC = pF 2.3 | % |
| 3 | AWCh3 | Available soil water capacity (volumetric fraction) with FC = pF 2.5 | % |
| 4 | Bldfie | Bulk density (fine earth) | kg/m3 |
| 5 | Cecsol | Cation Exchange Capacity of soil | cmolc/m3 |
| 6 | Clyppt | Weight percentage of the clay particles (<0.0002 mm) | % |
| 7 | Crfvol | Volumetric percentage of coarse fragments (>2 mm) | % |
| 8 | Ocdens | Soil organic carbon density | kg/m3 |
| 9 | Ocstha | Soil organic carbon stock | ton/ha |
| 10 | Orcdrc | Soil organic carbon content | Permille |
| 11 | Phihox | pH index measured in water solution | pH |
| 12 | Phikcl | pH index measured in KCl solution | pH |
| 13 | Sltppt | Weight percentage of the silt particles (0.0002–0.05 mm) | % |
| 14 | Sndppt | Weight percentage of the sand particles (0.05–2 mm) | % |
| 15 | Wwp | Available soil water capacity (volumetric fraction) until wilting point | % |
| 16 | mean_ST | Mean value of soil temperature | K |
| 17 | std_ST | Standard deviation of soil temperature | K |
| 18 | cv_ST | Coefficient of variance of soil temperature | / |

**Appendix Table 2.** Terrain data used to calibrate the soil model parameters

| ID | Name | Description | Units |
|---|---|---|---|
| 1 | dem_mean | Mean value of elevation | m |
| 2 | dem_std | Standard deviation of elevation | m |
| 3 | dem_cv | Coefficient of variance of elevation | / |
| 4 | Slope | Surface gradient | degree |
| 5 | TSC | Measure of surface upwards convexity | / |
| 6 | TST | Terrain surface texture | / |
| 7 | TRI | Terrain ruggedness index | / |
| 8 | PlanCur | Contour curvature | / |
| 9 | ProfCur | Slope profile curvature | / |

# References


Al-Yaari, A., Wigneron, J.P., Ciais, P., Reichstein, M., Ballantyne, A., Ogee, J., Ducharne, A., Swenson, J.J., Frappart, F., Fan, L., Wingate, L., Li, X., Hufkens, K., & Knapp, A.K. (2020). Asymmetric responses of ecosystem productivity to rainfall anomalies vary inversely with mean annual rainfall over the conterminous United States. *Glob Chang Biol, 26*, 6959-6973

Asner, G.P., Clark, J.K., Mascaro, J., Galindo García, G.A., Chadwick, K.D., Navarrete Encinales, D.A., Paez-Acosta, G., Cabrera Montenegro, E., Kennedy-Bowdoin, T., Duque, Á., Balaji, A., von Hildebrand, P., Maatoug, L., Phillips Bernal, J.F., Yepes Quintero, A.P., Knapp, D.E., García Dávila, M.C., Jacobson, J., & Ordóñez, M.F. (2012). High-resolution mapping of forest carbon stocks in the Colombian Amazon. *Biogeosciences, 9*, 2683-2696Attema, E.P.W., & Ulaby, F.T. (1978). Vegetation modeled as a water cloud. *Radio Science, 13*, 357-364

Baghdadi, N., Cerdan, O., Zribi, M., Auzet, V., Darboux, F., El Hajj, M., & Kheir, R.B. (2008). Operational performance of current synthetic aperture radar sensors in mapping soil surface

characteristics in agricultural environments: application to hydrological and erosion modelling. *Hydrological Processes, 22*, 9-20

Baghdadi, N., El Hajj, M., Zribi, M., & Bousbih, S. (2017). Calibration of the Water Cloud Model at C-Band for Winter Crop Fields and Grasslands. *Remote Sensing, 9*

Baghdadi, N.N., El Hajj, M., Zribi, M., & Fayad, I. (2016). Coupling SAR C-Band and Optical Data for Soil Moisture and Leaf Area Index Retrieval Over Irrigated Grasslands. *IEEE Journal of Selected Topics in Applied Earth Observations and Remote Sensing, 9*, 1229-1243

Bai, X., He, B., Li, X., Zeng, J., Wang, X., Wang, Z., Zeng, Y., & Su, Z. (2017). First Assessment of Sentinel-1A Data for Surface Soil Moisture Estimations Using a Coupled Water Cloud Model and Advanced Integral Equation Model over the Tibetan Plateau. *Remote Sensing, 9*, 714

Baur, M.J., Jagdhuber, T., Feldman, A.F., Akbar, R., & Entekhabi, D. (2019). Estimation of relative canopy absorption and scattering at L-, C- and X-bands. *Remote Sensing of Environment, 233*

Beck, H.E., Pan, M., Miralles, D.G., Reichle, R.H., Dorigo, W.A., Hahn, S., Sheffield, J., Karthikeyan, L., Balsamo, G., Parinussa, R.M., van Dijk, A.I.J.M., Du, J., Kimball, J.S., Vergopolan, N., & Wood, E.F. (2020). Evaluation of 18 satellite- and model-based soil moisture products using in situ measurements from 826 sensors

Berrisford, P., Kållberg, P., Kobayashi, S., Dee, D., Uppala, S., Simmons, A.J., Poli, P., & Sato, H. (2011). Atmospheric conservation properties in ERA-Interim. *Quarterly Journal of the Royal Meteorological Society, 137*, 1381-1399

Bindlish, R., & Barros, A.P. (2001). Parameterization of vegetation backscatter in radar-based, soil moisture estimation. *Remote Sensing of Environment, 76*, 130-137

Bracaglia, M., Ferrazzoli, P., & Guerriero, L. (1995). A fully polarimetric multiple scattering model for crops. *Remote Sensing of Environment, 54*, 170-179

Brandt, M., Wigneron, J.P., Chave, J., Tagesson, T., Penuelas, J., Ciais, P., Rasmussen, K., Tian, F., Mbow, C., Al-Yaari, A., Rodriguez-Fernandez, N., Schurgers, G., Zhang, W., Chang, J., Kerr, Y., Verger, A., Tucker, C., Mialon, A., Rasmussen, L.V., Fan, L., & Fensholt, R. (2018). Satellite passive microwaves reveal recent climate-induced carbon losses in African drylands. *Nat Ecol Evol, 2*, 827-835

878 Carreiras, J.M.B., Quegan, S., Le Toan, T., Ho Tong Minh, D., Saatchi, S.S., Carvalhais, N., Reichstein, M.,
879 & Scipal, K. (2017). Coverage of high biomass forests by the ESA BIOMASS mission under defense
880 restrictions. *Remote Sensing of Environment, 196*, 154-162
881 Chaparro, D., Duveiller, G., Piles, M., Cescatti, A., Vall-llossera, M., Camps, A., & Entekhabi, D.
882 (2019). Sensitivity of L-band vegetation optical depth to carbon stocks in tropical forests: a
883 comparison to higher frequencies and optical indices. *Remote Sensing of Environment,*
884 *232*Chaparro, D., Piles, M., Vall-llossera, M., Camps, A., Konings, A.G., & Entekhabi, D. (2018). L-
885 band vegetation optical depth seasonal metrics for crop yield assessment. *Remote Sensing of*
886 *Environment, 212*, 249-259
887 Chen, K.S., Tzong-Dar, W., Leung, T., Qin, L., Jiancheng, S., & Fung, A.K. (2003). Emission of rough
888 surfaces calculated by the integral equation method with comparison to three-dimensional moment
889 method simulations. *IEEE Transactions on Geoscience and Remote Sensing, 41*, 90-101
890 Chen, Y., Feng, X., & Fu, B. (2021). An improved global remote-sensing-based surface soil moisture
891 (RSSSM) dataset covering 2003–2018. *Earth System Science Data, 13*, 1-31Conrad, O., Bechtel, B.,
892 Bock, M., Dietrich, H., Fischer, E., Gerlitz, L., Wehberg, J., Wichmann, V., & Böhner, J. (2015). System
893 for Automated Geoscientific Analyses (SAGA) v. 2.1.4. *Geoscientific Model Development, 8*, 1991-
894 2007
895 Danielson, J.J., & Gesch, D.B. (2011). *Global multi-resolution terrain elevation data 2010 (GMTED2010).*
896 US Department of the Interior, US Geological Survey
897 Dente, L., Ferrazzoli, P., Su, Z., van der Velde, R., & Guerriero, L. (2014). Combined use of active and
898 passive microwave satellite data to constrain a discrete scattering model. *Remote Sensing of*
899 *Environment, 155*, 222-238
900 Didan, K. (2015). MOD13A1 MODIS/Terra Vegetation Indices 16-Day L3 Global 500m SIN Grid V006.
901 In: NASA EOSDIS Land Processes DAAC
902 DiMiceli, C., Carroll, M., Sohlberg, R., Kim, D.H., Kelly, M., & Townshend, J.R.G. (2015). MOD44B
903 MODIS/Terra Vegetation Continuous Fields Yearly L3 Global 250m SIN Grid V006. In: NASA
904 EOSDIS Land Processes DAAC

905 Dorigo, W., Himmelbauer, I., Aberer, D. et al. (2021). The International Soil Moisture Network: serving
906 Earth system science for over a decade. Hydrology and Earth system Science, in press,
907 https://doi.org/10.5194/hess-2021-2
908 Du, J., Kimball, J.S., Jones, L.A., Kim, Y., Glassy, J., & Watts, J.D. (2017). A global satellite environmental
909 data record derived from AMSR-E and AMSR2 microwave Earth observations. *Earth System Science*
910 *Data, 9*, 791-808
911 Dubois, P.C., van Zyl, J., & Engman, T. (1995). Measuring soil moisture with imaging radars. *IEEE*
912 *Transactions on Geoscience and Remote Sensing, 33*, 915-926
913 Duncanson, L., Neuenschwander, A., Hancock, S., Thomas, N., Fatoyinbo, T., Simard, M., Silva, C.A.,
914 Armston, J., Luthcke, S.B., Hofton, M., Kellner, J.R., & Dubayah, R. (2020). Biomass estimation from
915 simulated GEDI, ICESat-2 and NISAR across environmental gradients in Sonoma County, California.
916 *Remote Sensing of Environment, 242*
917 El Hajj, M., Baghdadi, N., Wigneron, J.-P., Zribi, M., Albergel, C., Calvet, J.-C., & Fayad, I. (2019). First
918 Vegetation Optical Depth Mapping from Sentinel-1 C-band SAR Data over Crop Fields. *Remote*
919 *Sensing, 11*
920 Entekhabi, D., Njoku, E.G., O'Neill, P.E., Kellogg, K.H., Crow, W.T., Edelstein, W.N., Entin, J.K.,
921 Goodman, S.D., Jackson, T.J., Johnson, J., Kimball, J., Piepmeier, J.R., Koster, R.D., Martin, N.,
922 McDonald, K.C., Moghaddam, M., Moran, S., Reichle, R., Shi, J.C., Spencer, M.W., Thurman, S.W.,
923 Tsang, L., & Van Zyl, J. (2010). The Soil Moisture Active Passive (SMAP) Mission. *Proceedings of the*
924 *IEEE, 98*, 704-716
925 Fan, L., Wigneron, J.P., Ciais, P., Chave, J., Brandt, M., Fensholt, R., Saatchi, S.S., Bastos, A., Al-Yaari, A.,
926 Hufkens, K., Qin, Y., Xiao, X., Chen, C., Myneni, R.B., Fernandez-Moran, R., Mialon, A., Rodriguez-
927 Fernandez, N.J., Kerr, Y., Tian, F., & Penuelas, J. (2019). Satellite-observed pantropical carbon
928 dynamics. *Nat Plants, 5*, 944-951
929 Fan, L., Wigneron, J.P., Xiao, Q., Al-Yaari, A., Wen, J., Martin-StPaul, N., Dupuy, J.L., Pimont, F., Al Bitar,
930 A., Fernandez-Moran, R., & Kerr, Y.H. (2018). Evaluation of microwave remote sensing for monitoring
931 live fuel moisture content in the Mediterranean region. *Remote Sensing of Environment, 205*, 210-223

Fan, L., Xiao, Q., Wen, J., Liu, Q., Jin, R., You, D., & Li, X. (2015). Mapping High-Resolution Soil Moisture over Heterogeneous Cropland Using Multi-Resource Remote Sensing and Ground Observations. *Remote Sensing, 7*, 13273-13297

Feldman, A.F., Akbar, R., & Entekhabi, D. (2018). Characterization of higher-order scattering from vegetation with SMAP measurements. *Remote Sensing of Environment, 219*, 324-338

Fernandez-Moran, R., Al-Yaari, A., Mialon, A., Mahmoodi, A., Al Bitar, A., De Lannoy, G., Rodriguez-Fernandez, N., Lopez-Baeza, E., Kerr, Y., & Wigneron, J.-P. (2017). SMOS-IC: An Alternative SMOS Soil Moisture and Vegetation Optical Depth Product. *Remote Sensing, 9*, 457

Ferrazzoli, P., Luzi, G., Paloscia, S., Pampaloni, P., Schiavon, G., & Solimini, D. (1989). Comarison between the microwave emissivity and backscatter coefficient of crops. *IEEE Transactions on Geoscience and Remote Sensing, 27*, 772-778

Figa-Saldaña, J., Wilson, J.J.W., Attema, E., Gelsthorpe, R., Drinkwater, M.R., & Stoffelen, A. (2014). The advanced scatterometer (ASCAT) on the meteorological operational (MetOp) platform: A follow on for European wind scatterometers. *Canadian Journal of Remote Sensing, 28*, 404-412

Forkel, M., Dorigo, W., Lasslop, G., Chuvieco, E., Hantson, S., Heil, A., Teubner, I., Thonicke, K., & Harrison, S.P. (2019). Recent global and regional trends in burned area and their compensating environmental controls. *Environmental Research Communications, 1*

Frappart, F., Wigneron, J.-P., Li, X., Liu, X., Al-Yaari, A., Fan, L., Wang, M., Moisy, C., Le Masson, E., Aoulad Lafkih, Z., Vallé, C., Ygorra, B., & Baghdadi, N. (2020). Global Monitoring of the Vegetation Dynamics from the Vegetation Optical Depth (VOD): A Review. *Remote Sensing, 12*

Frolking, S., Milliman, T., Palace, M., Wisser, D., Lammers, R., & Fahnestock, M. (2011). Tropical forest backscatter anomaly evident in SeaWinds scatterometer morning overpass data during 2005 drought in Amazonia. *Remote Sensing of Environment, 115*, 897-907

Fung, A.K., Li, Z., & Chen, K.S. (1992). Backscattering from a randomly rough dielectric surface. *IEEE Transactions on Geoscience and Remote Sensing, 30*, 356-369

Fung, A.K., & Eom, H. (1985). A Comparison between Active and Passive Sensing of Soil Moisture from Vegetated Terrains. *IEEE Transactions on Geoscience and Remote Sensing, GE-23*, 768-775

Grant, J.P., Wigneron, J.P., De Jeu, R.A.M., Lawrence, H., Mialon, A., Richaume, P., Al Bitar, A., Drusch, M., van Marle, M.J.E., & Kerr, Y. (2016). Comparison of SMOS and AMSR-E vegetation optical depth

961 to four MODIS-based vegetation indices. *Remote Sensing of Environment, 172*, 87-100Guio Blanco,
962 C.M., Brito Gomez, V.M., Crespo, P., & Ließ, M. (2018). Spatial prediction of soil water retention in a
963 Páramo landscape: Methodological insight into machine learning using random forest. *Geoderma, 316*,
964 100-114
965 Guyon, I., Weston, J., Barnhill, S., & Vapnik, V. (2002). Gene selection for cancer classification using
966 support vector machines. *Machine Learning, 46*, 389-422
967 Hahn, S., Reimer, C., Vreugdenhil, M., Melzer, T., & Wagner, W. (2017). Dynamic Characterization of the
968 Incidence Angle Dependence of Backscatter Using Metop ASCAT. *IEEE Journal of Selected Topics in*
969 *Applied Earth Observations and Remote Sensing, 10*, 2348-2359
970 Hengl, T., Mendes de Jesus, J., Heuvelink, G.B., Ruiperez Gonzalez, M., Kilibarda, M., Blagotic, A.,
971 Shangguan, W., Wright, M.N., Geng, X., Bauer-Marschallinger, B., Guevara, M.A., Vargas, R.,
972 MacMillan, R.A., Batjes, N.H., Leenaars, J.G., Ribeiro, E., Wheeler, I., Mantel, S., & Kempen, B.
973 (2017). SoilGrids250m: Global gridded soil information based on machine learning. *PLoS One, 12*,
974 e0169748
975 Hersbach, H., Stoffelen, A., & de Haan, S. (2007). An improved C-band scatterometer ocean geophysical
976 model function: CMOD5. *Journal of Geophysical Research, 112*
977 Hosseini, M., McNairn, H., Merzouki, A., & Pacheco, A. (2015). Estimation of Leaf Area Index (LAI) in
978 corn and soybeans using multi-polarization C- and L-band radar data. *Remote Sensing of Environment,*
979 *170*, 77-89
980 Huete, A., Didan, K., Miura, T., Rodriguez, E.P., Gao, X., & Ferreira, L.G. (2002). Overview of the
981 radiometric and biophysical performance of the MODIS vegetation indices. *Remote Sensing of*
982 *Environment, 83*, 195-213
983 Imaoka, K., Maeda, T., Kachi, M., Kasahara, M., Ito, N., & Nakagawa, K. (2012). Status of AMSR2
984 instrument on GCOM-W1. In, *Earth Observing Missions and Sensors: Development, Implementation,*
985 *and Characterization II* (p. 852815): International Society for Optics and Photonics
986 Jackson, T.J., & Schmugge, T.J. (1991). Vegetation effects on the microwave emission of soils. *Remote*
987 *Sensing of Environment, 36*, 203-212Jones, M.O., Jones, L.A., Kimball, J.S., & McDonald, K.C. (2011).
988 Satellite passive microwave remote sensing for monitoring global land surface phenology. *Remote*
989 *Sensing of Environment, 115*, 1102-1114

Karthikeyan, L., Pan, M., Konings, A.G., Piles, M., Fernandez-Moran, R., Nagesh Kumar, D., & Wood, E.F. (2019). Simultaneous retrieval of global scale Vegetation Optical Depth, surface roughness, and soil moisture using X-band AMSR-E observations. *Remote Sensing of Environment, 234*

Karthikeyan, L., Pan, M., Nagesh Kumar, D., & Wood, E.F. (2020). Effect of Structural Uncertainty in Passive Microwave Soil Moisture Retrieval Algorithm. *Sensors (Basel), 20*

Kerr, Y.H., Waldteufel, P., Wigneron, J.-P., Delwart, S., Cabot, F., Boutin, J., Escorihuela, M.-J., Font, J., Reul, N., Gruhier, C., Juglea, S.E., Drinkwater, M.R., Hahne, A., Martín-Neira, M., & Mecklenburg, S. (2010). The SMOS Mission: New Tool for Monitoring Key Elements ofthe Global Water Cycle. *Proceedings of the IEEE, 98*, 666-687

Koike, T., Nakamura, Y., Kaihotsu, I., Davaa, G., Matsuura, N., Tamagawa, K., & Fujii, H. (2004). Development of an Advanced Microwave Scanning Radiometer (Amsr-E) Algorithm for Soil Moisture and Vegetation Water Content. *Proceedings of Hydraulic Engineering, 48*, 217-222

Konings, A.G., & Gentine, P. (2017). Global variations in ecosystem-scale isohydricity. *Glob Chang Biol, 23*, 891-905

Konings, A.G., Piles, M., Rötzer, K., McColl, K.A., Chan, S.K., & Entekhabi, D. (2016). Vegetation optical depth and scattering albedo retrieval using time series of dual-polarized L-band radiometer observations. *Remote Sensing of Environment, 172*, 178-189

Konings, A.G., Yu, Y., Xu, L., Yang, Y., Schimel, D.S., & Saatchi, S.S. (2017). Active microwave observations of diurnal and seasonal variations of canopy water content across the humid African tropical forests. *Geophysical Research Letters*

Kottek, M., Grieser, J., Beck, C., Rudolf, B., & Rubel, F. (2006). World Map of the Köppen-Geiger climate classification updated. *Meteorologische Zeitschrift, 15*, 259-263

Lawrence, H., Wigneron, J.-P., Richaume, P., Novello, N., Grant, J., Mialon, A., Al Bitar, A., Merlin, O., Guyon, D., Leroux, D., Bircher, S., & Kerr, Y. (2014). Comparison between SMOS Vegetation Optical Depth products and MODIS vegetation indices over crop zones of the USA. *Remote Sensing of Environment, 140*, 396-406

Li, X., Al-Yaari, A., Schwank, M., Fan, L., Frappart, F., Swenson, J., & Wigneron, J.P. (2020a). Compared performances of SMOS-IC soil moisture and vegetation optical depth retrievals based on Tau-Omega and Two-Stream microwave emission models. *Remote Sensing of Environment, 236*

Li, X., Wigneron, J.-P., Frappart, F., Fan, L., Ciais, P., Fensholt, R., Entekhabi, D., Brandt, M., Konings, A.G., Liu, X., Wang, M., Al-Yaari, A., & Moisy, C. (2020b). Global-scale assessment and inter-comparison of recently developed/reprocessed microwave satellite vegetation optical depth products. *Remote Sensing of Environment*

Li, Y., Guan, K., Gentine, P., Konings, A.G., Meinzer, F.C., Kimball, J.S., Xu, X., Anderegg, W.R.L., McDowell, N.G., Martinez-Vilalta, J., Long, D.G., & Good, S.P. (2017). Estimating Global Ecosystem Isohydry/Anisohydry Using Active and Passive Microwave Satellite Data. *Journal of Geophysical Research: Biogeosciences, 122*, 3306-3321

Lievens, H., Martens, B., Verhoest, N.E.C., Hahn, S., Reichle, R.H., & Miralles, D.G. (2017). Assimilation of global radar backscatter and radiometer brightness temperature observations to improve soil moisture and land evaporation estimates. *Remote Sensing of Environment, 189*, 194-210

Liu, Y.Y., de Jeu, R.A.M., McCabe, M.F., Evans, J.P., & van Dijk, A.I.J.M. (2011). Global long-term passive microwave satellite-based retrievals of vegetation optical depth. *Geophysical Research Letters, 38*

Liu, Y.Y., van Dijk, A.I.J.M., de Jeu, R.A.M., Canadell, J.G., McCabe, M.F., Evans, J.P., & Wang, G. (2015). Recent reversal in loss of global terrestrial biomass. *Nature Climate Change, 5*, 470-474

Liu, Y.Y., van Dijk, A.I.J.M., McCabe, M.F., Evans, J.P., & de Jeu, R.A.M. (2013). Global vegetation biomass change (1988-2008) and attribution to environmental and human drivers. *Global Ecology and Biogeography, 22*, 692-705

Ma, C., Li, X., & McCabe, M.F. (2020). Retrieval of High-Resolution Soil Moisture through Combination of Sentinel-1 and Sentinel-2 Data. *Remote Sensing, 12*

Ma, C.F., Li, X., & Wang, S.G. (2015). A Global Sensitivity Analysis of Soil Parameters Associated With Backscattering Using the Advanced Integral Equation Model. *IEEE Transactions on Geoscience and Remote Sensing, 53*, 5613-5623

Mankou, G.S., Ligot, G., Loubota Panzou, G.J., Boyemba, F., Loumeto, J.J., Ngomanda, A., Obiang, D., Rossi, V., Sonke, B., Yongo, O.D., & Fayolle, A. (2021). Tropical tree allometry and crown allocation, and their relationship with species traits in central Africa. *Forest Ecology and Management, 493*Moesinger, L., Dorigo, W., de Jeu, R., van der Schalie, R., Scanlon, T., Teubner, I., & Forkel, M. (2020). The global long-term microwave Vegetation Optical Depth Climate Archive (VODCA). *Earth System Science Data, 12*, 177-196

1048 Myneni, R., Knyazikhin, Y., & Park, T. (2015). MCD15A2H MODIS/Terra+Aqua Leaf Area Index/FPAR
1049 8-day L4 Global 500m SIN Grid V006. In: NASA EOSDIS Land Processes DAAC
1050 Naeimi, V., Scipal, K., Bartalis, Z., Hasenauer, S., & Wagner, W. (2009). An Improved Soil Moisture
1051 Retrieval Algorithm for ERS and METOP Scatterometer Observations. *IEEE Transactions on*
1052 *Geoscience and Remote Sensing, 47*, 1999-2013
1053 Oh, Y., Sarabandi, K., & Ulaby, F.T. (1992). An empirical model and an inversion technique for radar
1054 scattering from bare soil surfaces. *IEEE Transactions on Geoscience and Remote Sensing, 30*, 370-381
1055 Owe, M., de Jeu, R., & Holmes, T. (2008). Multisensor historical climatology of satellite-derived global land
1056 surface moisture. *Journal of Geophysical Research, 113*
1057 Owe, M., de Jeu, R., & Walker, J. (2001). A methodology for surface soil moisture and vegetation optical
1058 depth retrieval using the microwave polarization difference index. *IEEE Transactions on Geoscience*
1059 *and Remote Sensing, 39*, 1643-1654
1060 Parrens, M., Al Bitar, A., Mialon, A., Fernandez-Moran, R., Ferrazzoli, P., Kerr, Y., & Wigneron, J.P. (2017).
1061 Estimation of the L-Band Effective Scattering Albedo of Tropical Forests Using SMOS Observations.
1062 *Ieee Geoscience and Remote Sensing Letters, 14*, 1223-1227
1063 Parrens, M., Wigneron, J.-P., Richaume, P., Mialon, A., Al Bitar, A., Fernandez-Moran, R., Al-Yaari, A., &
1064 Kerr, Y.H. (2016). Global-scale surface roughness effects at L-band as estimated from SMOS
1065 observations. *Remote Sensing of Environment, 181*, 122-136
1066 Patton, J., & Hornbuckle, B. (2013). Initial Validation of SMOS Vegetation Optical Thickness in Iowa. *Ieee*
1067 *Geoscience and Remote Sensing Letters, 10*, 647-651
1068 Pedregosa, F., Varoquaux, G., Gramfort, A., Michel, V., Thirion, B., Grisel, O., Blondel, M., Prettenhofer,
1069 P., Weiss, R., Dubourg, V., Vanderplas, J., Passos, A., Cournapeau, D., Brucher, M., Perrot, M., &
1070 Duchesnay, E. (2011). Scikit-learn: Machine Learning in Python. *Journal of Machine Learning*
1071 *Research, 12*, 2825-2830
1072 Pfeil, I., Wagner, W., Forkel, M., Dorigo, W., & Vreugdenhil, M. (2020). Does ASCAT observe the spring
1073 reactivation in temperate deciduous broadleaf forests? *Remote Sensing of Environment, 250*
1074 Potapov, P., Li, X., Hernandez-Serna, A., Tyukavina, A., Hansen, M.C., Kommareddy, A., Pickens, A.,
1075 Turubanova, S., Tang, H., Silva, C.E., Armston, J., Dubayah, R., Blair, J.B., & Hofton, M. (2020).

Mapping global forest canopy height through integration of GEDI and Landsat data. *Remote Sensing of Environment*

Pulliainen, J.T., Heiska, K., Hyyppa, J., & Hallikainen, M.T. (1994). Backscattering properties of boreal forests at the C- and X-bands. *IEEE Transactions on Geoscience and Remote Sensing, 32*, 1041-1050

Qiu, S., Lin, Y., Shang, R., Zhang, J., Ma, L., & Zhu, Z. (2018). Making Landsat Time Series Consistent: Evaluating and Improving Landsat Analysis Ready Data. *Remote Sensing, 11*, 51

Qin, Y., Xiao, X., Wigneron, J.-P., Ciais, P., Brandt, M., Fan, L., Li, X., Crowell, S., Wu, X., Doughty, R., Zhang, Y., Liu, F., Sitch, S., & Moore, B. (2021). Carbon loss from forest degradation exceeds that from deforestation in the Brazilian Amazon. *Nature Climate Change*

Quesney, A. (2000). Estimation of Watershed Soil Moisture Index from ERS/SAR Data. *Remote Sensing of Environment, 72*, 290-303

Rao, K., Anderegg, W.R.L., Sala, A., Martínez-Vilalta, J., & Konings, A.G. (2019). Satellite-based vegetation optical depth as an indicator of drought-driven tree mortality. *Remote Sensing of Environment, 227*, 125-136

Rodríguez-Fernández, N.J., Mialon, A., Mermoz, S., Bouvet, A., Richaume, P., Al Bitar, A., Al-Yaari, A., Brandt, M., Kaminski, T., Le Toan, T., Kerr, Y.H., & Wigneron, J.-P. (2018). An evaluation of SMOS L-band vegetation optical depth (L-VOD) data sets: high sensitivity of L-VOD to above-ground biomass in Africa. *Biogeosciences, 15*, 4627-4645

Saatchi, S.S., Harris, N.L., Brown, S., Lefsky, M., Mitchard, E.T., Salas, W., Zutta, B.R., Buermann, W., Lewis, S.L., Hagen, S., Petrova, S., White, L., Silman, M., & Morel, A. (2011). Benchmark map of forest carbon stocks in tropical regions across three continents. *Proc Natl Acad Sci U S A, 108*, 9899-9904

Santoro, M., Beaudoin, A., Beer, C., Cartus, O., Fransson, J.E.S., Hall, R.J., Pathe, C., Schmullius, C., Schepaschenko, D., Shvidenko, A., Thurner, M., & Wegmüller, U. (2015). Forest growing stock volume of the northern hemisphere: Spatially explicit estimates for 2010 derived from Envisat ASAR. *Remote Sensing of Environment, 168*, 316-334

Santoro, M., & Cartus, O. (2019). ESA Biomass Climate Change Initiative (Biomass_cci): Global datasets of forest above-ground biomass for the year 2017, v1. In: Centre for Environmental Data Analysis

Shamambo, D.C., Bonan, B., Calvet, J.-C., Albergel, C., & Hahn, S. (2019). Interpretation of ASCAT Radar Scatterometer Observations Over Land: A Case Study Over Southwestern France. *Remote Sensing, 11*

1105 Simard, M., Pinto, N., Fisher, J.B., & Baccini, A. (2011). Mapping forest canopy height globally with
1106 spaceborne lidar. *Journal of Geophysical Research, 116*
1107 Steele-Dunne, S.C., Friesen, J., & van de Giesen, N. (2012). Using Diurnal Variation in Backscatter to Detect
1108 Vegetation Water Stress. *IEEE Transactions on Geoscience and Remote Sensing, 50*, 2618-2629
1109 Stoffelen, A., & Anderson, D. (1997). Scatterometer Data Interpretation: Measurement Space and Inversion.
1110 *Journal of Atmospheric and Oceanic Technology, 14*, 1298-1313
1111 Sulla-Menashe, D., & Friedl, M. (2019). MCD12Q1 MODIS/Terra+Aqua Land Cover Type Yearly L3
1112 Global 500m SIN Grid V006. In: NASA EOSDIS Land Processes DAAC
1113 Teubner, I.E., Forkel, M., Camps-Valls, G., Jung, M., Miralles, D.G., Tramontana, G., van der Schalie, R.,
1114 Vreugdenhil, M., Mösinger, L., & Dorigo, W.A. (2019). A carbon sink-driven approach to estimate gross
1115 primary production from microwave satellite observations. *Remote Sensing of Environment, 229*, 100-
1116 113
1117 Teubner, I.E., Forkel, M., Jung, M., Liu, Y.Y., Miralles, D.G., Parinussa, R., van der Schalie, R.,
1118 Vreugdenhil, M., Schwalm, C.R., Tramontana, G., Camps-Valls, G., & Dorigo, W.A. (2018). Assessing
1119 the relationship between microwave vegetation optical depth and gross primary production.
1120 *International Journal of Applied Earth Observation and Geoinformation, 65*, 79-91
1121 Tian, F., Wigneron, J.P., Ciais, P., Chave, J., Ogee, J., Penuelas, J., Raebild, A., Domec, J.C., Tong, X.,
1122 Brandt, M., Mialon, A., Rodriguez-Fernandez, N., Tagesson, T., Al-Yaari, A., Kerr, Y., Chen, C.,
1123 Myneni, R.B., Zhang, W., Ardo, J., & Fensholt, R. (2018). Coupling of ecosystem-scale plant water
1124 storage and leaf phenology observed by satellite. *Nat Ecol Evol, 2*, 1428-1435
1125 Togliatti, K., Hartman, T., Walker, V.A., Arkebauer, T.J., Suyker, A.E., VanLoocke, A., & Hornbuckle,
1126 B.K. (2019). Satellite L–band vegetation optical depth is directly proportional to crop water in the
1127 US Corn Belt. *Remote Sensing of Environment, 233*Ulaby, F., Batlivala, P., & Dobson, M. (1978).
1128 Microwave Backscatter Dependence on Surface Roughness, Soil Moisture, and Soil Texture: Part I-Bare
1129 Soil. *IEEE Transactions on Geoscience Electronics, 16*, 286-295
1130 Ulaby, F.T., Sarabandi, K., McDonald, K., Whitt, M., & Dobson, M.C. (2007). Michigan microwave canopy
1131 scattering model. *International Journal of Remote Sensing, 11*, 1223-1253

1132 Verhoest, N.E., Lievens, H., Wagner, W., Alvarez-Mozos, J., Moran, M.S., & Mattia, F. (2008). On the Soil
1133 Roughness Parameterization Problem in Soil Moisture Retrieval of Bare Surfaces from Synthetic
1134 Aperture Radar. *Sensors (Basel), 8*, 4213-4248
1135 Vreugdenhil, M., Dorigo, W.A., Wagner, W., de Jeu, R.A.M., Hahn, S., & van Marle, M.J.E. (2016).
1136 Analyzing the Vegetation Parameterization in the TU-Wien ASCAT Soil Moisture Retrieval. *IEEE*
1137 *Transactions on Geoscience and Remote Sensing, 54*, 3513-3531
1138 Vreugdenhil, M., Hahn, S., Melzer, T., BauerMarschallinger, B., Reimer, C., Dorigo, W.A., & Wagner, W.
1139 (2017). Assessing Vegetation Dynamics Over Mainland Australia With Metop ASCAT. *IEEE Journal*
1140 *of Selected Topics in Applied Earth Observations and Remote Sensing, 10*, 2240-2248
1141 Vreugdenhil, M., Navacchi, C., Bauer-Marschallinger, B., Hahn, S., Steele-Dunne, S., Pfeil, I., Dorigo, W.,
1142 & Wagner, W. (2020). Sentinel-1 Cross Ratio and Vegetation Optical Depth: A Comparison over
1143 Europe. *Remote Sensing, 12*
1144 Wagner, W., Hahn, S., Kidd, R., Melzer, T., Bartalis, Z., Hasenauer, S., Figa-Saldaña, J., de Rosnay, P., Jann,
1145 A., Schneider, S., Komma, J., Kubu, G., Brugger, K., Aubrecht, C., Züger, J., Gangkofner, U.,
1146 Kienberger, S., Brocca, L., Wang, Y., Blöschl, G., Eitzinger, J., & Steinnocher, K. (2013). The ASCAT
1147 Soil Moisture Product: A Review of its Specifications, Validation Results, and Emerging Applications.
1148 *Meteorologische Zeitschrift, 22*, 5-33
1149 Wagner, W., Lemoine, G., & Rott, H. (1999a). A Method for Estimating Soil Moisture from ERS
1150 Scatterometer and Soil Data. *Remote Sensing of Environment, 70*, 191-207
1151 Wagner, W., Noll, J., Borgeaud, M., & Rott, H. (1999b). Monitoring soil moisture over the Canadian Prairies
1152 with the ERS scatterometer. *IEEE Transactions on Geoscience and Remote Sensing, 37*, 206-216
1153 Wigneron, J.P., Ferrazzoli, P., Calvet, J.C., & Bertuzzi, P. (1999). A parametric study on passive and active
1154 microwave observations over a soybean crop. *IEEE Transactions on Geoscience and Remote Sensing,*
1155 *37*, 2728-2733
1156 Wigneron, J.-P., Fouilhoux, M., Prévot, L., Chanzy, A., Olioso, A., Baghdadi, N., & King, C. (2002).
1157 Monitoring sunflower crop development from C-band radar observations. *Agronomie, 22*, 587-595
1158 Wigneron, J.-P., Li, X., Frappart, F., Fan, L., Al-Yaari, A., De Lannoy, G., Liu, X., Wang, M., Le Masson,
1159 E., & Moisy, C. (2021). SMOS-IC data record of soil moisture and L-VOD: Historical development,
1160 applications and perspectives. *Remote Sensing of Environment, 254*

1161 Wigneron, J.P., Fan, L., Ciais, P., Bastos, A., Brandt, M., Chave, J., Saatchi, S., Baccini, A., & Fensholt, R.
1162 (2020). Tropical forests did not recover from the strong 2015-2016 El Nino event. *Sci Adv, 6*, eaay4603
1163 Wigneron, J.P., Jackson, T.J., O'Neill, P., De Lannoy, G., de Rosnay, P., Walker, J.P., Ferrazzoli, P.,
1164 Mironov, V., Bircher, S., Grant, J.P., Kurum, M., Schwank, M., Munoz-Sabater, J., Das, N., Royer, A.,
1165 Al-Yaari, A., Al Bitar, A., Fernandez-Moran, R., Lawrence, H., Mialon, A., Parrens, M., Richaume, P.,
1166 Delwart, S., & Kerr, Y. (2017). Modelling the passive microwave signature from land surfaces: A review
1167 of recent results and application to the L-band SMOS & SMAP soil moisture retrieval algorithms.
1168 Remote Sensing of Environment, 192, 238-262
1169 Wigneron, J.P., Waldteufel, P., Chanzy, A., Calvet, J.C., & Kerr, Y. (2000). Two-Dimensional Microwave
1170 Interferometer Retrieval Capabilities over Land Surfaces (SMOS Mission). *Remote Sensing of*
1171 *Environment, 73*, 270-282
1172 Zribi, M., Muddu, S., Bousbih, S., Al Bitar, A., Tomer, S.K., Baghdadi, N., & Bandyopadhyay, S. (2019).
1173 Analysis of L-Band SAR Data for Soil Moisture Estimations over Agricultural Areas in the Tropics.
1174 *Remote Sensing, 11*
1175